

A SURVEY OF RO-VIBRATIONAL CO SPECTRA FROM PROTOPLANETARY
DISKS WITH ISHELL ON THE NASA IRTF TELESCOPE

by

Kirsten Marie Abernathy, B.S.

A thesis submitted to the Graduate Council of
Texas State University in partial fulfillment
of the requirements for the degree of
Master of Science
with a Major in Physics
May 2023

Committee Members:

Andrea Banzatti, Chair

Blagoy Rangelov

Aditya Togi

COPYRIGHT

by

Kirsten Marie Abernathy

2023

DEDICATION

This work is dedicated to my family and friends that have constantly been a source of support and encouragement.

ACKNOWLEDGMENTS

I would like to thank my advisor and committee chair, Andrea Banzatti, for his consistent support and guidance throughout this research project and my research as an undergraduate. I'd also like to thank my other committee members, Dr.Rangelov and Dr.Togi for their support in the final stages of this project.

TABLE OF CONTENTS

	Page
LIST OF TABLES.....	vii
LIST OF FIGURES.....	viii
ABSTRACT.....	x
CHAPTER	
I. INTRODUCTION.....	1
I.I Protoplanetary Disks.....	1
I.II Molecular Spectroscopy.....	7
I.III Gas Kinematics.....	10
I.IV Summary of Previous Works.....	12
II. SAMPLE AND DATA REDUCTION.....	24
II.I Sample.....	24
II.II Data Reduction.....	29
II.II.I Flat Fielding.....	30
II.II.II Wavelength Calibration.....	31
II.II.III Spectral Extraction.....	33
II.II.IV Combining Spectra.....	36
II.II.V Telluric Correction.....	37
III. SLAB MODEL AND FITTING PROCEDURE.....	39
III.I Slab Model.....	39
III.II Rotation Diagrams.....	40
III.III Line Decomposition.....	43
IV. RESULTS AND DISSCUSSION.....	45
V. CONCLUSION.....	56

REFERENCES.....58

LIST OF TABLES

	Page
Table 1. Summary of key papers on CO emission in protoplanetary disks.....	22
Table 2. $^{12}\text{CO } v = 1 - 0$ slab model fit results.....	51
Table 3. $^{12}\text{CO } v = 2 - 1$ slab model fit results.....	53
Table 4. $^{12}\text{CO } v = 1 - 0$ and $v = 2 - 1$ slab model fit results.....	54
Table 5. $^{13}\text{CO } v = 1 - 0$ slab model fit results.....	55

LIST OF FIGURES

	Page
Figure 1. Spectral energy distributions (SEDs) and corresponding illustrations of the protostar and pre-main sequence stages.....	2
Figure 2. Simplified structure of a protoplanetary disk including details about dust and gas.....	4
Figure 3. Spectral energy distributions (SEDs) and corresponding illustrations of dust emission in full, pre-transitional, and transitional disks.....	5
Figure 4. Energy ladder for rovibrational spectra.....	8
Figure 5. Illustration of a model generated CO spectra.....	10
Figure 6. Doppler broadening of line profiles due to the rotation of a disk.....	11
Figure 7. Model line profiles of a ring of gas in Keplerian rotation at different radii.....	11
Figure 8. Examples of fundamental CO spectra of T Tauri stars observed with NIRSPEC.....	13
Figure 9. Slab model results and rotation diagrams for CO emission.....	15
Figure 10. Example of CO line profiles.....	18
Figure 11. Gallery of line profile types calculated by averaging the observed $^{12}\text{CO } v = 1 - 0$ lines between R(10) and P(32).....	19
Figure 12. Overview of the two line profile types and their emitting regions based on observed kinematics and excitation.....	21
Figure 13. Spectral coverage comparison, preliminary sample, and rotation diagram comparison of instrument coverage.....	25
Figure 14. CO line shape parameter S as a function of T_{eff} , disk inclination, and infrared index.....	26
Figure 15. Histograms showing stellar and disk sample properties.....	27

Figure 16. Overview of line profiles observed in this iSHELL survey.....	28
Figure 17. Xspextool calibration window for generating flat fields and wavelength calibration.....	30
Figure 18. Xspextool wavelength calibration.....	32
Figure 19. Example of the AB observing method used to isolate the science target and remove background emission.....	33
Figure 20. Xspextool point source spectral extraction window.....	34
Figure 21. Xspextool point source extraction fitting the spatial profiles by order.....	35
Figure 22. Xspextool point source extraction fitting the spatial profiles by order corresponding with each order shown on the detector.....	37
Figure 23. Xtellcorr window.....	38
Figure 24. Example of the rotation diagram technique applied to CO spectra.....	41
Figure 25. The rotation diagram technique applied to different ranges of $v=1-0$ lines.....	42
Figure 26. Best-fit model results for Figure 25.....	42
Figure 27. Examples of the stacked line profiles and decomposition into a broad component (BC) and narrow component (NC) where present.....	43
Figure 28. Slab model fit for AS 205 N BC with the best fitting model results.....	45
Figure 29. Two segments of the spectra observed for AS 205 N.....	46
Figure 30. CO kinematics for various components.....	48
Figure 31. ^{12}CO fit results for $v = 1 - 0$ (V1) and $v = 2 - 1$ (V2) temperature and column density compared to CO FWHM.....	49
Figure 32. Slab model results for $^{12}\text{CO } v = 1 - 0$, $^{12}\text{CO } v = 2 - 1$, and $^{13}\text{CO } v = 1 - 0$	50

ABSTRACT

Protoplanetary disks around pre-main-sequence stars are the birthplace of planets and planetary systems. The fundamental CO rovibrational band at $\sim 4.7 \mu\text{m}$ is the most ubiquitous and easily observed tracer of gas in the inner disk region of protoplanetary disks, due to the sensitivity to warm temperatures (300-1500 K). When observed at high resolving power, CO spectra reveals both the kinematics and excitation of gas in planet-forming regions, and their evolution with time. After 20 years of studies of warm CO gas in disks with previous instruments, here at Texas State we have led a new survey with iSHELL on the NASA IRTF telescope in Hawaii, with the 0.375" and 0.75" slit widths that provide the unprecedented combination of large spectral coverage of 4.52–5.25 μm in one single exposure and high spectral resolution of $R \sim 60\text{-}90\text{k}$. With iSHELL, we remotely observed CO rovibrational spectra of ~ 70 protoplanetary disks, reaching an unprecedented high-quality and large sample. I will present how we reduced the spectra and fitted them as single or broad and narrow components for $^{12}\text{CO } v = 1 - 0, v = 2 - 1$, and where present $^{13}\text{CO } v = 1 - 0$ with a simple slab model. I will report the model fit results and discuss their correlation analysis in the context of stellar parameters and disk properties to illustrate the new properties that this survey is revealing.

I. INTRODUCTION

The formation of stars and planets is a widely studied field in astronomy. As a young star forms, a protoplanetary disk forms around it, these two objects coexist and influence the evolution of each other. These interactions set initial conditions that impact the evolution of a mature system like the Solar System. Disks supply material to the central star and forming protoplanets. Therefore, studying protoplanetary disks is key to understanding the environments where planets form and how they form. In this thesis, I systematically reduce and analyze molecular gas emission to provide an overview of diverse excitation conditions and trends.

I.I Protoplanetary Disks

The star formation process begins when a cold dense molecular cloud collapses, eventually forming a warm core embedded in an envelope of gas and dust. Disks form along with protostars due to the gas having too much angular momentum to fall directly onto the protostar (Armitage 2010). Young stellar objects (YSOs) are classified into four classes based on their spectral energy distribution (SED, see Figure 1). Class 0 sources represent the earliest stages of a collapsing molecular cloud, where any protostar is deeply embedded within optically thick gas and dust. The protostar is embedded such that the SED peaks in the far-IR with no flux being detected in the near-IR. Class I sources are still embedded in an envelope that dominates the emission. The SED peaks between near- and mid-IR. Class II sources are in a later stage of evolution when the envelope has been accreted onto the pre-main sequence (PMS) star and disk. The SED peaks between near- and mid-IR, UV and IR excess in the SED signify the presence of a

disk (Armitage 2010). Class III sources represent YSOs whose disks have dissipated leaving a PMS star with little to no disk material remaining. At this stage the SED is dominated by the PMS star, some show evidence of a debris disk that is gas poor. In this thesis, we focus on class II sources.

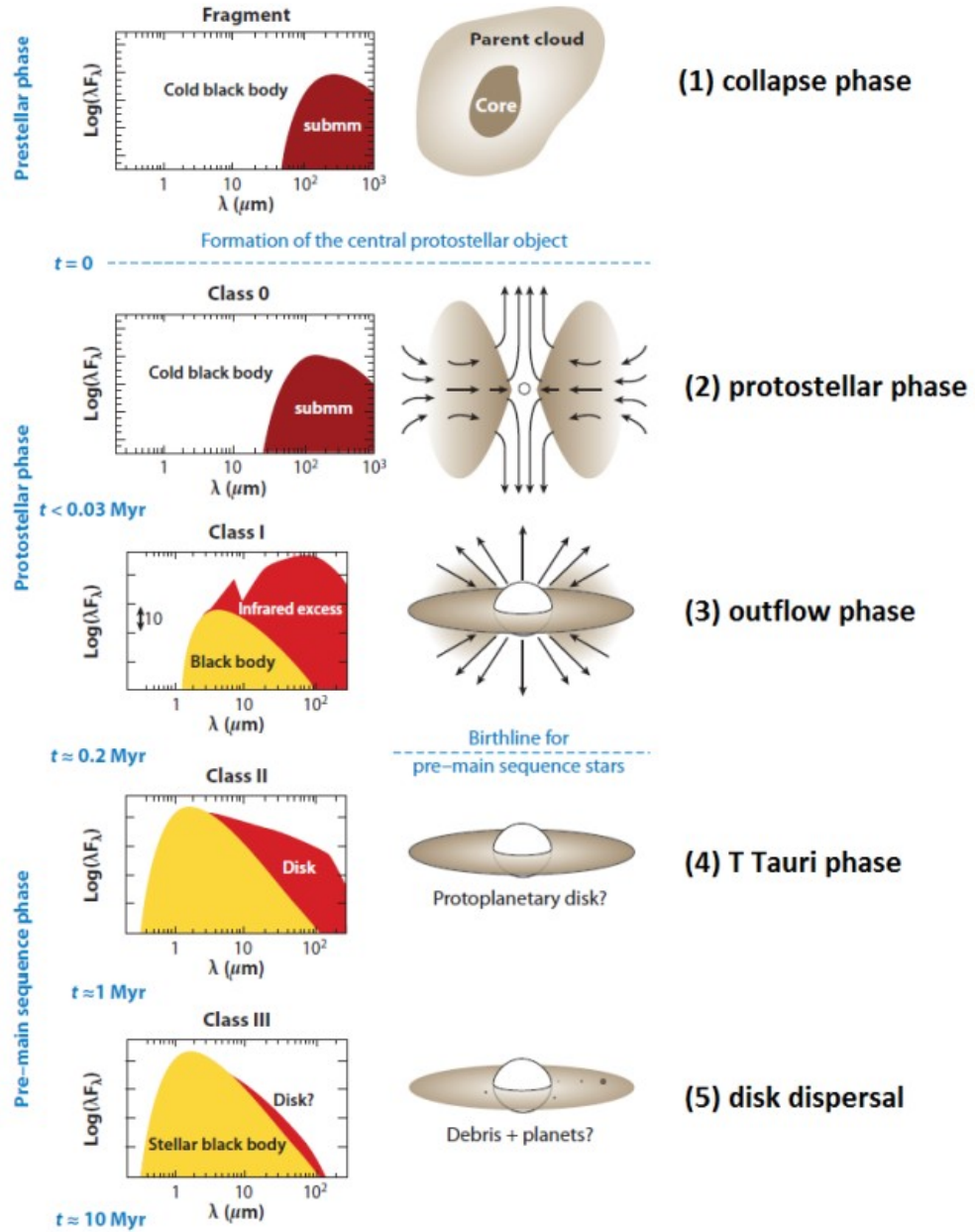


Figure 1. Spectral energy distributions (SEDs) and corresponding illustrations of the protostar and pre-main sequence stages (From Dauphas and Chaussidon 2011)

Protoplanetary disks around young stars are the birthplace of planets, making class II objects particularly interesting since it is the best phase to see the star and disk, additionally this is when planets are thought to be forming. Class II objects can be further classified between Herbig Ae/Be and T Tauri stars. T Tauri stars (TTs) are young stars with mass around $1.5 M_{\odot}$ and below; classical T Tauri (cTTS) include a large number of broad UV and optical emission lines that are dominated by H α . TTs exhibit excess continuum flux in the UV due to shocks associated with accretion; IR excess from heated dust within the protoplanetary disk; furthermore, they are known to exhibit both regular and erratic variability in their emission (Stahler and Palla 2004). Herbig Ae/Be (HAeBe) stars are objects with intermediate masses ranging from $2-8 M_{\odot}$ that exhibit some degree of excess IR emission. Young protoplanetary disks are “gas rich” and referred to as “full” disks; there are several spectral diagnostics to observe gas in disks from the inner, hotter region out to the outer, colder region. The radial temperature gradient implies that this range of regions is observed across the electromagnetic spectrum from the infrared out to radio wavelengths (see Figure 2).

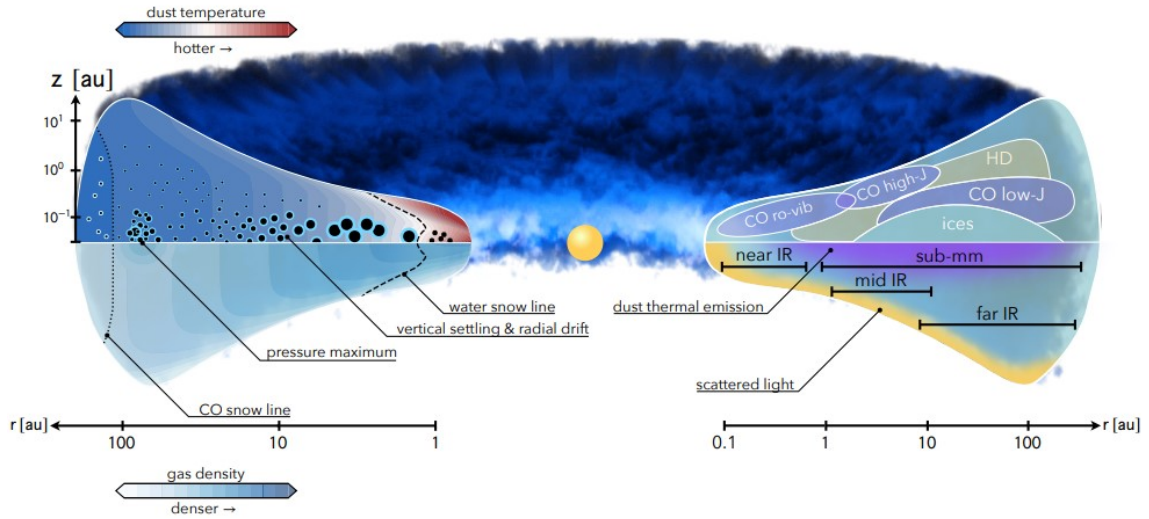


Figure 2. Simplified structure of a protoplanetary disk including details about dust and gas. Left: an illustration showing dust size, dust temperature, and gas density structure throughout the disk. Right: shows a simplified representation of various emission regions within a disk (From Miotello et al. 2022).

“Transitional” disks, instead, are a subset of disks whose SEDs show a deficit of infrared excess due to a central hole or gap in the dust emission. This deficit can be small near-infrared and/or mid-infrared excess with significant mid- or far-infrared excess indicating that the radial structure of the dust includes an inner hole (Espaillat et al. 2014, and Figure 3). Transitional disks are believed to be a more evolved disk with an inner hole possibly due to tidal effects from a companion star or a planet clearing dust in the inner disk. Pre-transitional disks are those which feature a gap rather than a hole in the inner disk and are believed to be an important phase of disk evolution and important for studying disk dissipation. The presence of such a gap or hole can be characterized by the infrared index between $13\ \mu\text{m}$ and $30\ \mu\text{m}$, n_{13-30} , as measured from the observed SED (see Figure 3). The sample in this thesis is a combination of Class II objects: TTs, HAeBe, and transitional disks (see section on sample below).

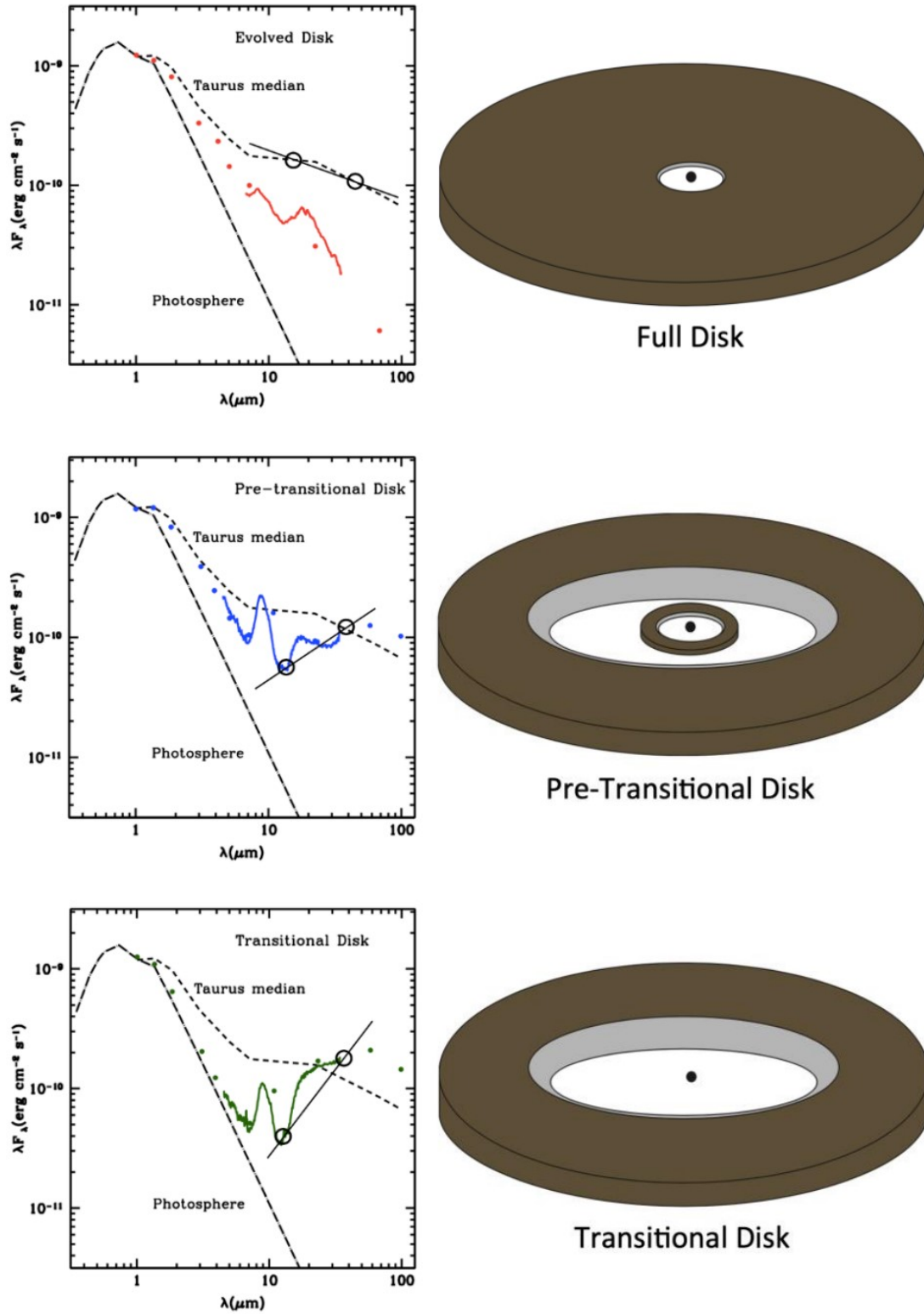


Figure 3. Spectral energy distributions (SEDs) and corresponding illustrations of dust emission in full, pre-transitional, and transitional disks. The slope of the spectral index,

n_{13-30} , is shown in each SED as a black line intersecting two open circles located at 13 μm and 30 μm (Original figure from Espaillat et al. 2014, modified by Sanchez 2021).

While dust is a minor portion of the total disk mass, it dominates the opacity making dust easier to observe. Due to this, most observational constraints are deduced from studying dust emission (Carmona 2010). Scattered light and continuum emission from dust is sensitive to the physical conditions and distribution of solids within the disk. Scattered light originates from $\sim\mu\text{m}$ sized dust grains at a suitable altitude in the disk atmosphere (see Figure 2) reflecting radiation emitted by the host star and is sensitive to radial variation of vertical height of the disk with a resolution of 30-50 milliarcseconds (Andrews 2020). The main challenge of scattered light is contrast with the host star that prevents measurements of the innermost disk (~ 10 AU), sensitivity at larger radii due to the dilution of the stellar radiation field. Solids within the disk emit a thermal continuum that spans a wide range of wavelengths (1 μm - 1cm). Most of the emission is optically thick and acts as a temperature diagnostic. Optical depth (τ_ν) decreases with wavelength, leading to $\tau_\nu \leq 1$, which is expected for sub-mm. In this optically thin limit, intensity scales with the surface density of solids and has a sensitive dependence on properties of solid particles. Overall, this tracer is bright, accessible at high resolution and unlike scattered light, has no limitations based on stellar contrast. Most of the knowledge about disk structure is based on sub-mm continuum observations (recently from ALMA). However, there are some disadvantages including lack of detailed particle properties and the validity of the optically thin approximation.

Properties such as the amount of dust and size of particles are crucial for theoretical models of planet formation. Dust size determines how they interact with gas

and how they may accumulate to eventually assemble the building blocks of planets. The total amount of dust determines if there is enough material for forming terrestrial planets or cores of giant planets (Miotello et al. 2022).

I.II Molecular Spectroscopy

Molecular spectroscopy allows for environments in space to be studied due to interactions between electromagnetic waves and matter. Molecules, like atoms, have discrete, quantized energy levels spaced out according to their properties and geometry. An emission line will be produced when a molecule transitions from a high energy level to a lower energy level and a photon that corresponds to the difference between energy levels is emitted. Similarly, a photon of a specific energy is absorbed for a molecule to transition from a lower energy state to a higher energy state. Using the Born-Oppenheimer approximation, the total energy of a molecule can be written as:

$$\Delta E = E_e + E_{vib} + E_{rot}$$

Where, E_e , E_{vib} , E_{rot} are electronic energy, vibrational energy and rotational energy respectively, and $E_e \gg E_{vib} \gg E_{rot}$. Rotational energy levels are denoted by the rotational quantum number J , that takes integer values $J = 0, 1, 2, \dots$ for ground and excitations. Allowed pure rotational transitions follow the selection rule $\Delta J = J'' - J' = \pm 1, 0$, where J'' denotes the upper energy level and J' denotes a lower energy level.

Vibrational energy levels are denoted by the vibrational quantum number ν , that takes on integer values $\nu = 0, 1, 2, \dots$ for ground and excitations. Allowed fundamental vibrational transitions follow the selection rule $\Delta \nu = \nu'' - \nu' = \pm 1$, where ν'' denotes the upper energy level and ν' denotes a lower energy level. In ro-vibrational spectra, vibrational

transitions and rotational transitions occur in conjunction, for a given vibrational transition changes in J occur. For the fundamental vibrational transition $\nu = 1$, $\Delta J = 1$ or $\Delta J = -1$. When $\Delta J = 1$, the R branch is formed, and the P branch is formed when $\Delta J = -1$ (see Figure 4). These rotational transitions happening between $\nu = 1$ and $\nu = 0$ form the $\nu = 1 - 0$ band. The naming convention for transitions of in a rovibrational spectra specify which branch and the J'' of the transition. For example the first transition of the P-branch is P(1) and the first transition of the R-branch is R(0).

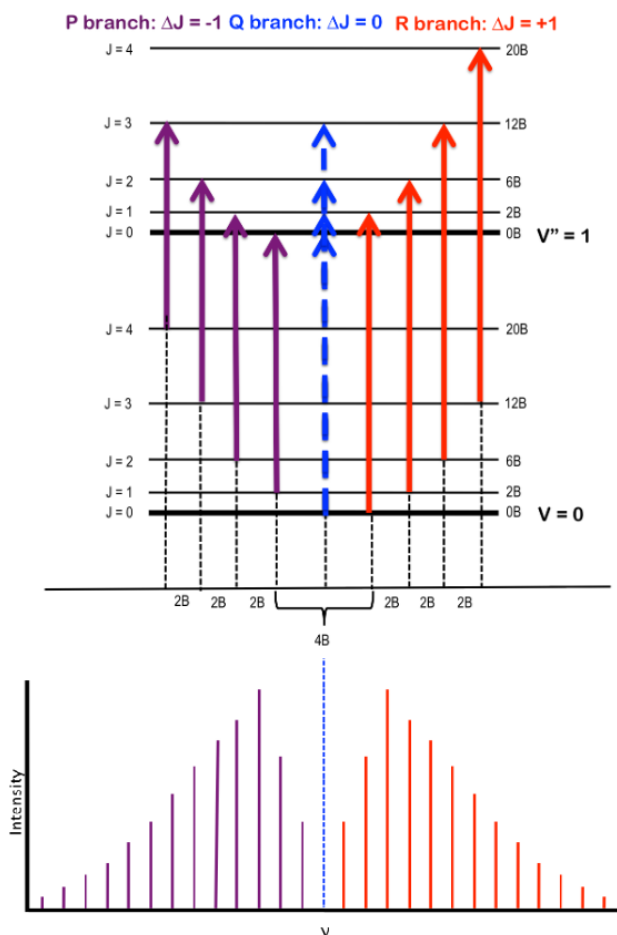


Figure 4. Energy ladder for rovibrational spectra. Top: rovibrational energy levels with the P-branch shown in purple, the R-branch shown in red, and the theoretical Q-branch line in blue. The arrows indicate rotational transitions that happen within the $\nu = 1 - 0$

band. Bottom: Ideal rovibrational spectrum, where each line is a transition corresponding with a change in the rovibrational energy levels of the top panel (From Libretexts.org).

The most abundant molecule in space is H_2 , it is difficult to observe due to the lack of a permanent dipole moment. CO is the second most abundant molecule and is easier to observe when compared to H_2 . The fundamental CO rovibrational band at $4.7 \mu m$ is effectively the best tracer of the inner disk region of protoplanetary disks. Additionally, due to the dissociation energy of CO being 11.16 eV, the molecule is stable and long-lived. CO emission at $4.7 \mu m$ probes temperatures ranging from ~ 300 K-1500 K, covering the region where terrestrial planets form (Carmona 2010). The main isotopologue of CO, ^{12}CO , is very abundant in disks such that its emission is mostly optically thick and provides kinematic information (Miotello et al. 2022). In observed and model spectra there is visible overlap of the $^{12}CO v = 1 - 0$ band, $^{12}CO v = 2 - 1$ band, and $^{13}CO v = 1 - 0$ band as shown in Figure 5. This overlap between vibrational bands can lead to blending of lines, the spikes seen on the $^{12}CO v = 1 - 0$ bands in Figure 5 are due to blending with $^{12}CO v = 2 - 1$ lines.

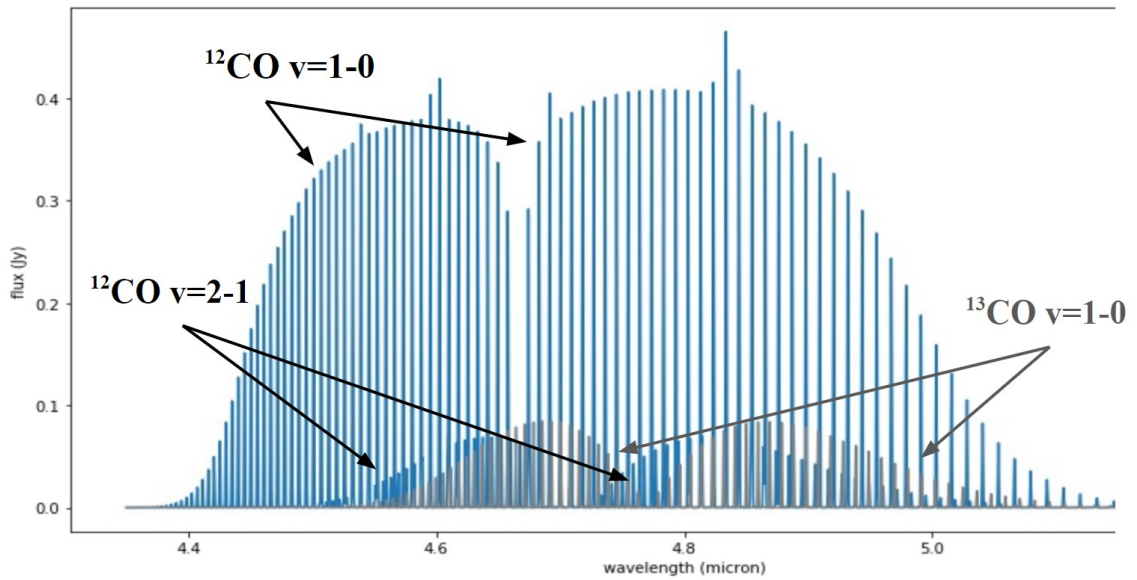


Figure 5. Illustration of a model generated CO spectra. The overlap between the $^{12}\text{CO } \nu = 1 - 0$, $^{12}\text{CO } \nu = 2 - 1$, and $^{13}\text{CO } \nu = 1 - 0$ vibrational bands even in models is noticeable. The most prominent feature is the $^{12}\text{CO } \nu = 1 - 0$ band, while the $^{12}\text{CO } \nu = 2 - 1$ band is weaker and offset in comparison. $^{13}\text{CO } \nu = 1 - 0$ is shown in light grey and is offset from $^{12}\text{CO } \nu = 1 - 0$ due to the change in mass of ^{13}CO .

I.III Gas Kinematics

Kinematics of observed gas impact the molecular emission line profiles. The doppler effect introduces line broadening; the faster gas is moving towards or away from the observer, the broader the line will appear (Figure 6). The velocity component of rotation towards the observer produces a line to become blue shifted and velocity component of rotation away from the observer produces a redshifted line. These shifts blend with the line observed when all the velocity is translational, giving rise to an overall broader line profile.

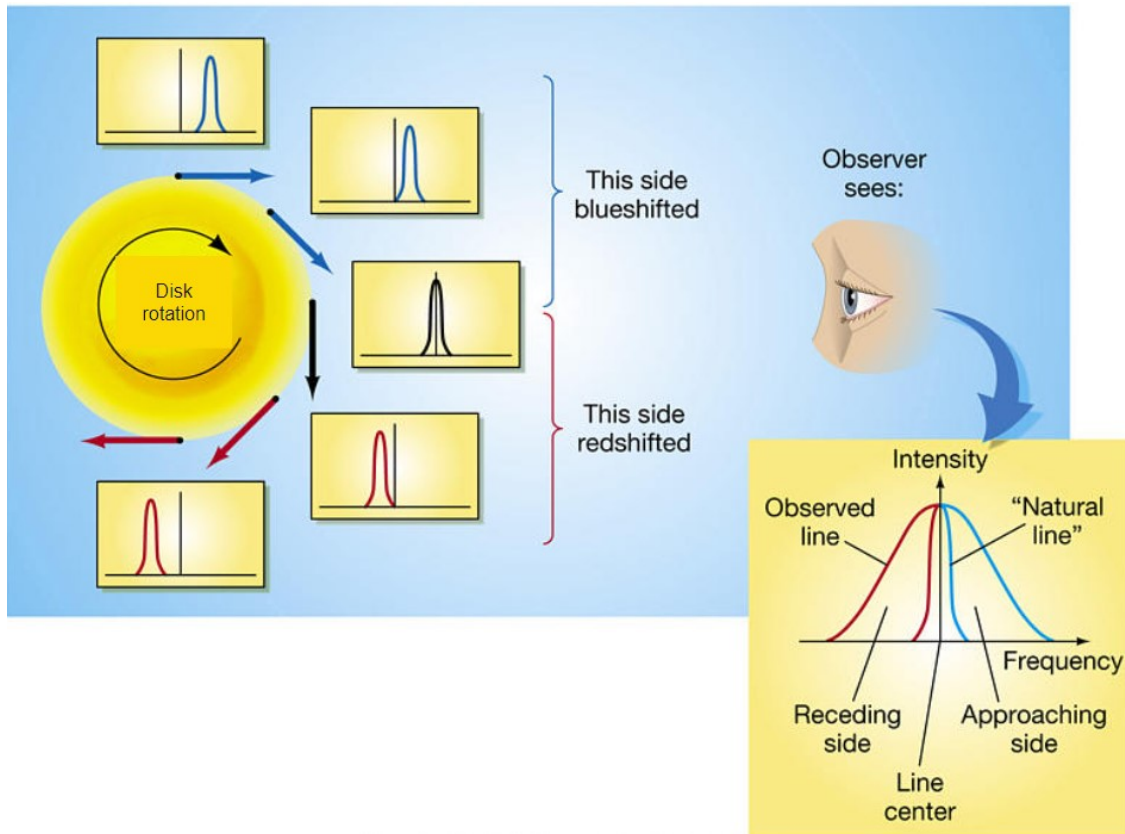


Figure 6. Doppler broadening of line profiles due to the rotation of a disk.

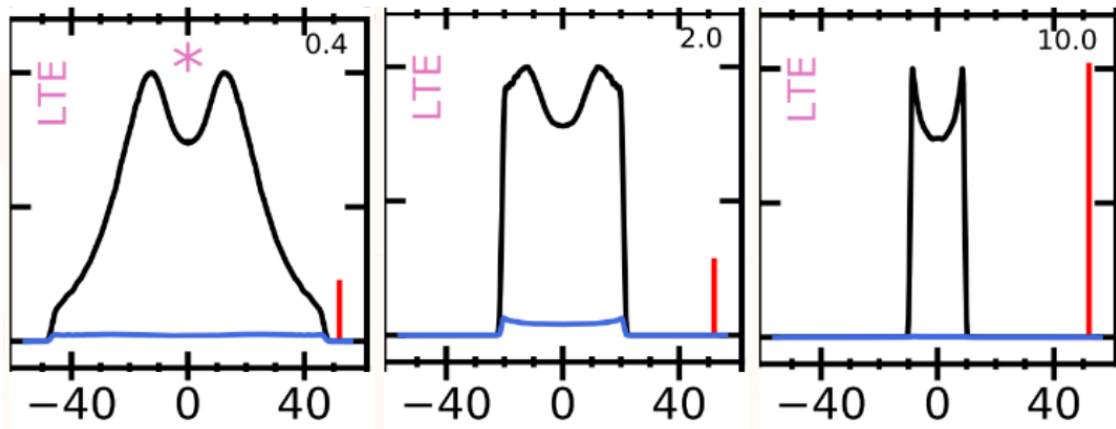


Figure 7. Model line profiles of a ring of gas in Keplerian rotation at different radii: 0.4 AU, 2 AU, and 10 AU (From Bosman et al. 2019).

A ring of gas in Keplerian rotation produces a characteristic double-peaked line profile (Figure 7). Assuming Keplerian motions allows for the line width to trace a Keplerian velocity, which indicates where emission originates from within a disk. Line width decreases as the location of the emitting gas moves to larger radii further away from the protostar. Broad features arise from faster gas closer to the protostar, while narrow features arise from slower moving gas at a larger radius.

I.IV Summary of Previous Works

CO spectra from protoplanetary disks have been studied since 2003 in several papers, of which I provide a brief overview of in this section, summarized in Table 1.

Najita et al. 2003 reported the results of a high-resolution spectroscopic survey of CO fundamental emission of eighteen T Tauri stars (Figure 8) observed with CSHELL (R~20000) and NIRSPEC (R~25000). They find that CO fundamental emission is commonly detected in T Tauri stars, and the emission is likely from the disk due to the generally symmetric line profile and line profile widths. Furthermore, the emission strength appears to be correlated with accretion tracers. They suggest significant CO emission appears in low column density regions and temperature inversion regions. High excitation temperatures (~1000K) and potentially significant optical depth are found in some sources. The high temperature of the gas suggests that the surface gas component of the inner disk region may be heated more than the surface dust components. Their observations of gap regions and circumstellar disks of binaries confirm ongoing accretion of disk material after the formation of gaps in the disk. They also suggest that with the

high range of excitation temperature and column densities that can be probed with the fundamental CO emission and its isotopes, dynamics and physical properties of the inner disk regions may be probed with the fundamental emission.

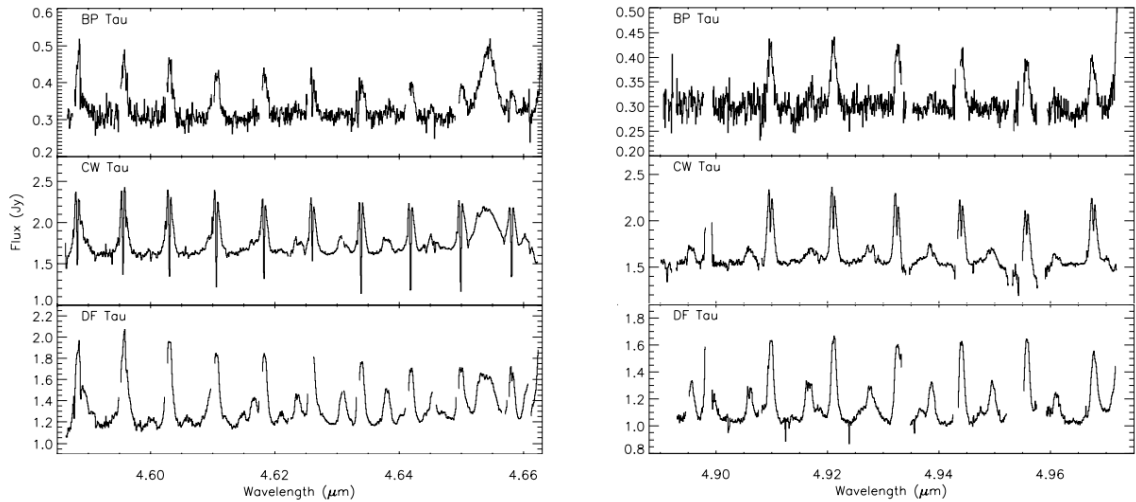


Figure 8. Examples of fundamental CO spectra of T Tauri stars observed with NIRSPEC (From Najita et al. 2003)

Salyk et al. 2009 analyzed NIRSPEC high-resolution ($R \sim 25000$) CO rovibrational spectra detected in nine of the fourteen transitional disks within their sample. This work focuses on disks that have depleted, or optically thin, inner regions with optically thick outer regions. The spectra obtained using NIRSPEC includes two orders spanning $4.65\text{--}4.78\ \mu\text{m}$ and $4.96\text{--}5.1\ \mu\text{m}$, including the fundamental ^{12}CO rovibrational fundamental transitions $R(0\text{--}1)$ and $P(1\text{--}12, 30\text{--}40)$, as well as, portions of the $v = 2 - 1$ spectrum and ^{13}CO . They use spatially resolved spectra to determine the inner extent of CO emission and find that most of these disks have CO emission originating from within the optically thin gap. For eight of the disks within the sample where CO was detected and had enough lines detected they fit the emission using a

simple slab model to find a temperature, column density and emitting area that describe the gas.

Salyk et al. 2011 b used a large sample of CO spectra most of which were obtained with NIRSPEC to probe the inner disk structure of Herbig Ae/Be and classical T Tauri stars. These observations are part of a larger NIRSPEC survey of protoplanetary disks spanning from 2001-2010, portions of this sample have been previously presented in other works (Blake & Boogert 2004; Salyk et al. 2007, 2009, 2011a). They use a simple parameterization of CO emission as a function of disk radius and report that R_{CO} can be determined and is similar to the stellar corotation radii for low mass stars but significantly larger than the stellar corotation radii for HAeBe stars. Inner CO radii strongly correlated with the system luminosity and consistent with dust sublimation radii. CO line fluxes were fitted using a simple LTE slab model, described in Salyk et al. 2009, to describe the emission with a single temperature, CO column density, and emitting area. These results were used to generate rotation diagrams shown in Figure 9. Column densities were constrained using ^{13}CO detections and non-detections. They reported finding a systematically lower temperature for transitional disks and Herbig stars compared to T Tauri stars. Rotational temperatures were found to be similar or slightly lower than expected temperature of blackbody grains at the inner CO radius.

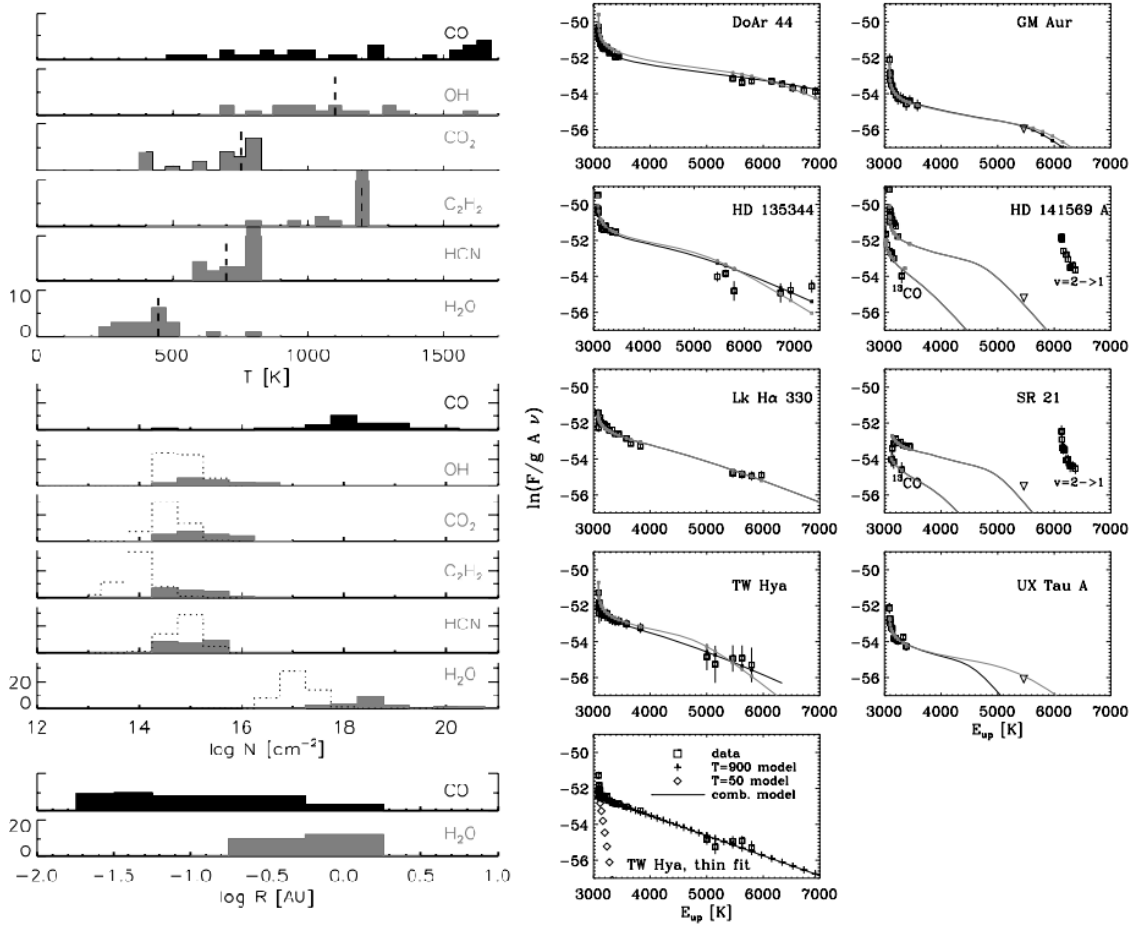


Figure 9. Slab model results and rotation diagrams for CO emission. Left: histograms showing the distribution best-fit model parameters for various molecules, with the histograms for CO in black. Dotted unfilled histograms show upper limits and dashed vertical lines show the assumed temperature used to compute the upper limits. Right: rotation diagrams for sources with CO emission, where measured fluxes are shown as open boxes, triangles denote upper limits, and filled squares connected by solid lines are the best-fit model (left figure from Salyk 2011a, right figure from Salyk 2009).

van der Plas et al. 2015 sought to determine the spatial distribution of the CO gas and physical properties for a sample of 13 Herbig stars. Of these objects 12 had detected CO rovibrational emission using CRIFES on the VLT. They found that the flaring disks, also referred to as group I disks, within this sample show highly excited CO fundamental emission. While self-shadowed disks, also referred to as group II disks, show emission

that isn't as highly excited. Using a similar approach as Salyk et al. 2009, CO fluxes were fitted with an isothermal slab model to determine the temperature, column density, and the emitting area. The rotational temperature of ^{13}CO is found to be lower than that of ^{12}CO . They report CO emission in group I sources originating from larger distances when compared to group II disks. This sample shows no correlation between the line shape and excitation, or self-shadowed (group II) and flaring disks (group I). However, they detected a broadening of emission lines as a function of excitation temperature for two of their group II disks: HD 98922 and HD 135344B. Classifying most of their other group II disks was difficult due to limitations on the S/N, while group I disks do not show trend in higher vibrational bands. They propose thermal or pumping by IR radiation as the dominant excitation mechanism behind the CO vibrational band populations for group II disks. While for group I disks fluorescence is believed to be the mechanism, as well as suggesting that the presence of fluorescence in disks could be an indicator for the presence of moderately sized gaps in their disks.

Brittain et al. 2007 obtained high-resolution CO spectra of fourteen intermediate-mass young stars using NIRSPEC ($R \sim 25000$). Their sample includes two intermediate mass T Tauri stars, seven Herbig Ae/Be stars, four transitional Herbig, and one embedded intermediate mass source that is not definitively classified. They report a 100% detection rate of rovibrational CO for disks with an optically thick inner disk. While for the five disks that do not have an optically thick inner disk, rovibrational CO was only detected in HD 141569. The detection of CO in HD 141569 is shown to be accounted for through UV fluorescence of CO. The first key result from this study is that

in HAeBe stars, thermally excited CO closely traces dust in the inner disk. Second, for optically thin disks UV fluoresced CO may assist in constraining the mass and timescale of depletion of gas in the inner disk region of disks that are slightly more evolved.

Hercezeg et al. 2011 presented VLT/CRIRES high-resolution ($R=90000$) spectra for 18 low-mass YSOs, of which CO was detected in 14. They find emission lines can be classified into a broad warm component and a narrow cool component (see Figure 10). The narrow emission was found to be typically detected from embedded objects with high bolometric luminosity. Broad CO emission was found to be frequently detected in YSO with a bolometric luminosity of $< 15 L_{\odot}$. The broad emission shares properties seen in mature disks around CTTS and is attributed to warm (1000K) gas within the inner disk. The lack of CO emission detected from objects with bolometric luminosities of $< 15 L_{\odot}$ is suggested to be due to either a lack of warm CO gas in the inner disk due to photodissociation, or the disk has not yet settled into Keplerian rotation. Narrow CO emission lines tend to be cooler (300 - 400K), with some showing a slight blueshift indicating an origin in a slow outflow. They also note that 6 objects show winds in CO absorption with velocities ranging from 10 to 100 $km s^{-1}$ and temperatures of $1260 \pm 100 K$, indicating the presence of a molecular wind launched from the disk.

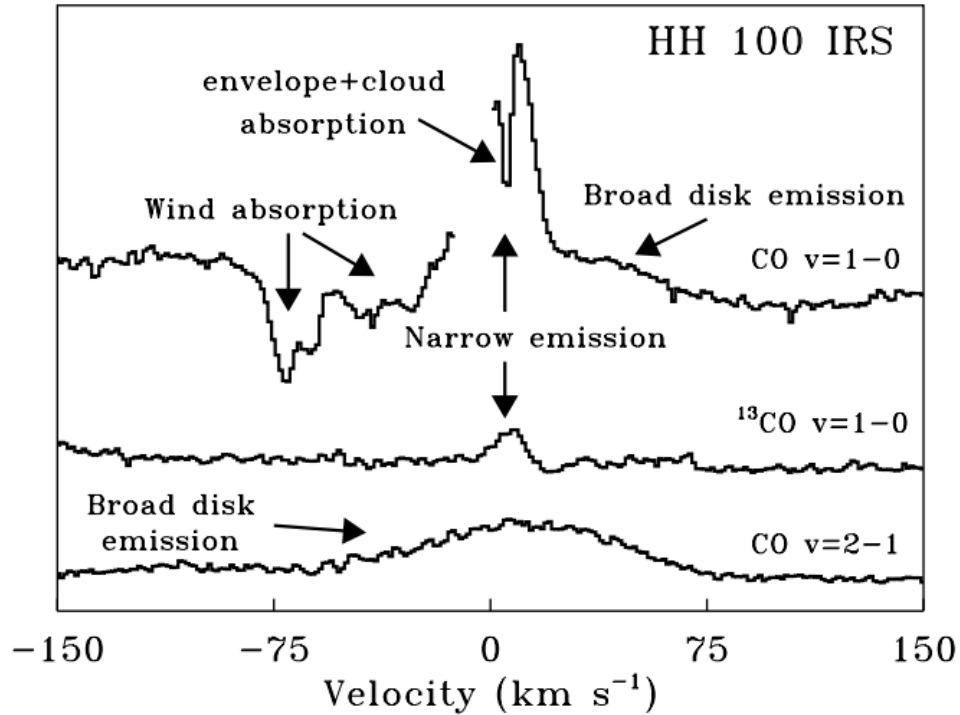


Figure 10. Example of CO line profiles. $^{12}\text{CO } v = 1 - 0$, $v = 2 - 1$, and $^{13}\text{CO } v = 1 - 0$ lines profiles for HH 100 IRS observed using VLT/CRIRES. Each observed component is identified with a physical region (From Hercezug et al. 2011)

Brown et al. 2013 presented a large survey of rovibrational CO including 69 protoplanetary disks and 22 embedded protostars obtained with CRIRES on the ESO Very Large Telescope (R~95000) to trace warm gas in planet-forming regions around young stars. The high resolution of this survey provides new insight into the kinematics of the gas through line profiles (see Figure 11). Sources with clean emission were sorted into four categories based on their full width half maximum (FWHM): (1) narrow, (2) broad single peaked, (3) broad, and (4) double peaked. Absorption line profiles were also categorized: (5) unresolved absorption, (6) broad central absorption, (7) blue absorption, and (8) absorption with blue emission. In this sample, pure double-peaked Keplerian line profiles are uncommon. They report most line profiles show wings consistent with

Keplerian rotation in the inner disk, however a majority have excess flux at the center of the line. They found that models require additional emission from larger radii to replicate this emission. They conclude that slow disk winds may be a common feature of young stars that are traceable with CO due to their observation of a trend with slight excess emission on the blue sides of the lines. Weak emission lines from ^{13}CO were detected, in general tracing cooler gas than ^{12}CO . This emission may arise from further out in the disk as suggested by narrow line profiles. Additionally, a high fraction ($\sim 50\%$) of the sources exhibit vibrationally excited emission, which is consistent with UV fluorescent excitation.

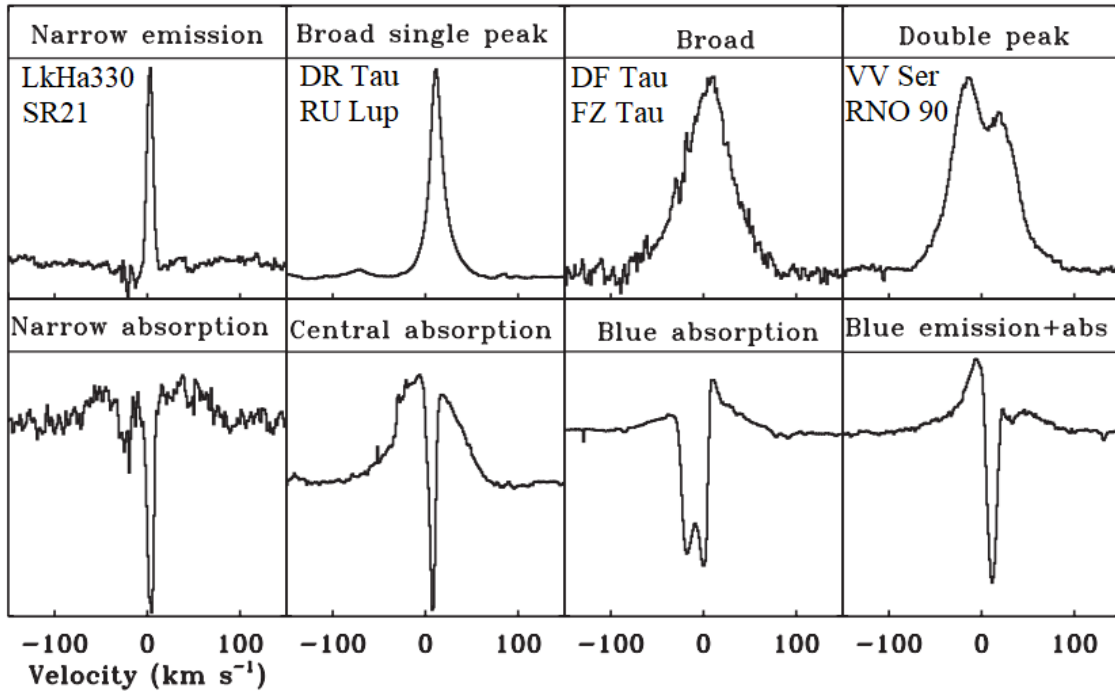


Figure 11. Gallery of line profile types calculated by averaging the observed $^{12}\text{CO } \nu = 1 - 0$ lines between R(10) and P(32). Disks included in Brown et al. 2013 and this work are indicated on the top panels (From Brown et al. 2013).

Banzatti et al. 2022 presented an overview of a M-band spectroscopic survey of 31 protoplanetary disks obtained with IRTF-iSHELL ($R \sim 60,000\text{-}92,000$), which has a coverage of $4.52\text{--}5.24\ \mu\text{m}$, including >50 lines from the R and P branches of ^{12}CO and ^{13}CO , and combined to another 30 disks from the previous CRIRES survey for a total sample of 61. The rich data provides unprecedented information on the excitation of multiple emission and absorption components. CO emission was categorized into two fundamental categories based on line profile shapes: double peaked lines interpreted as emission from Keplerian rings, and triangular lines from the disk surface plus a low-velocity part of a wind (see Figure 12). These profiles were then decomposed and fit as a single component (SC) or a double component including a narrow component (NC) and broad component (BC). Notable findings of this survey include: the first detection of a large fraction of double peaked lines in M-band CO emission, first observation of M-band CO at resolution $R > 50,000$ for 15 disks, first detection of two separate Keplerian rings of CO emission in a disk at $< 2\ \text{AU}$ (in HD 259431), first detection of common CO kinematic variability over timescales between 1-14 years, and the first detection of H_2O lines near $5\ \mu\text{m}$ in a disk (in AS 205 N).

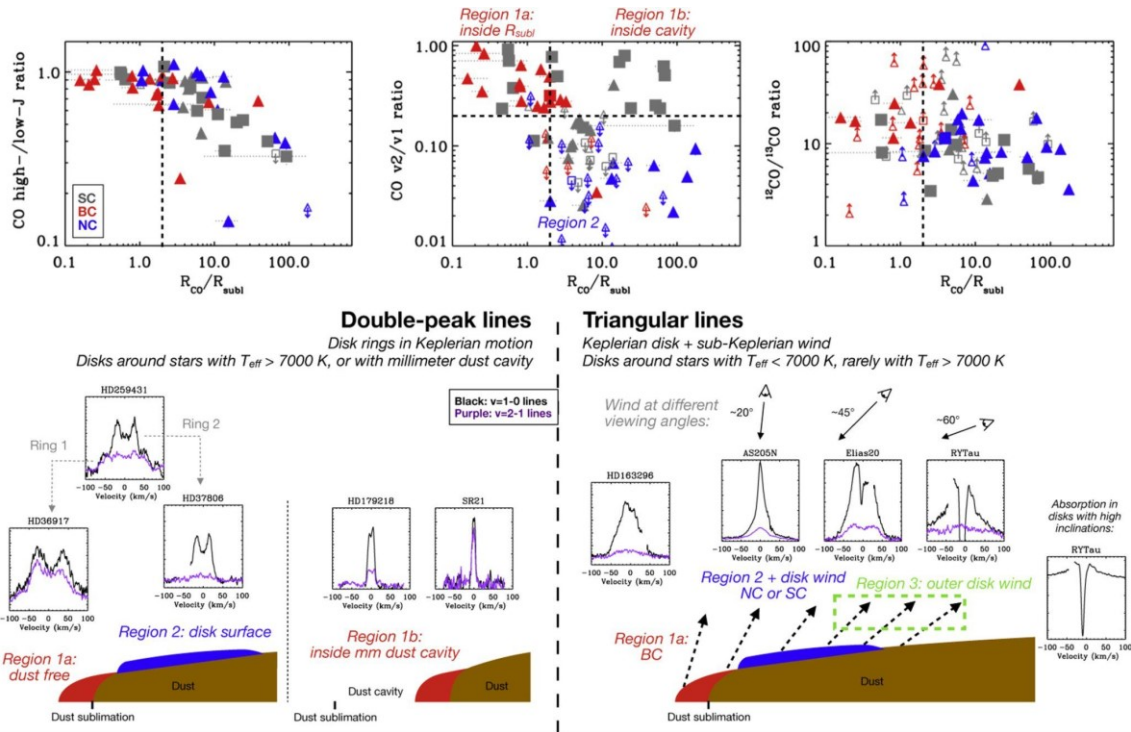


Figure 12. Overview of the two line profile types and their emitting regions based on observed kinematics and excitation. The symbols indicate the line shape parameter (described section III.3 of this work). Colors correspond to the different line components: SC (grey), BC (red), NC (blue) and abs (green). Low-J is defined as the J levels between 5 and 18 for the P and R-branch. High-J is defined at the J levels between 25 and 31 in the P branch (From Banzatti et al. 2022).

To summarize, CO spectra has been analyzed over 20 years as a tool to study protoplanetary disks with samples that have increased over time. This work has shown that CO is commonly detected as a tracer of warm inner disks and led to a complex classification of four types of emission lines. Interpretations have simplified the classification of emission profiles into two categories: triangular and double-peaked lines.

Table 1. Summary of key papers on CO emission in protoplanetary disks.

Paper	Sample	Instrument	Spectral Resolution	Spectral Coverage (μm)	Key results
Najita et al. 2003	18 TTs (one transitional)	CSHELL, NIRSPEC	20000, 25000	4.65-4.78	CO emission commonly detected in TTs and is likely originates from the disk
Salyk et al. 2009	14 transitional disks	NIRSPEC	25000	4.65-4.78	CO emission is observed within an optically thin gap, implying that CO survives in the dust cavity
Salyk et al. 2011 b	32 disks (Herbig, TTs, and transitional disks)	NIRSPEC	25000	4.65-4.78	CO temperature is systematically lower in transitional disks and Herbig's compared to TTs
Brittain et al. 2007	14 intermediate mass stars (2 TTS, 7 Herbig's, 4 transitional Herbig's, 1 embedded)	NIRSPEC	25000	4.65-4.78	100% detection rate of rovibrational CO in disks with an optically thick inner disk. In Herbig's thermally excited CO traces dust in the inner disk
Herczeg et al. 2011	18 low-mass YSOs with dense envelopes	CRIRES	90000	4.65-4.75	Class 0/I objects have more complex CO line profiles. Classification of emission lines into two categories: broad warm component and narrow cold component
Brown et al. 2013	69 disks	CRIRES	95000	4.65-4.75	CO is classified into 4 categories: narrow, broad single peaked, broad, and double peaked. Absorption classified into: unresolved abs, broad central, blue abs, and abs with blue emission
van der Plas et al. 2015	13 Herbig's	CRIRES	94000	4.65-4.75	Rotational temperature of ^{13}CO is lower than ^{12}CO . CO emission from group I sources originate from larger radii than in group II disks

Paper	Sample	Instrument	Spectral Resolution	Spectral Coverage (μm)	Key results
Banzatti et al. 2022	31 disks (mostly Herbig) + 30 disks with CRIRES (mostly TTs)	iSHELL + CRIRES	60000 – 94000	4.52-5.24	CO classified into 2 categories: double peaked and triangular, interpreted as purely disk vs disk+wind emission

II. SAMPLE AND DATA REDUCTION

In the following chapter I will describe our sample of protoplanetary disks. As a part of my work, I have reduced a majority of this iSHELL sample and will summarize the data reduction process using IRTF's Spextool pipeline.

II.I Sample

The sample analyzed in this work includes 64 protoplanetary disks around pre-main sequence stars observed with IRTF-iSHELL, with the 0.375" and 0.75" slits, resolution of $R \sim 60,000$ -92,000, covering 4.52–5.25 μm in one single exposure, shown in Figure 13 in comparison to the spectral coverage of VLT-CRIRES and Keck-NIRSPEC. This includes part of the rovibrational R branch and the entire P branch of the CO fundamental band ($\Delta v = 1$).

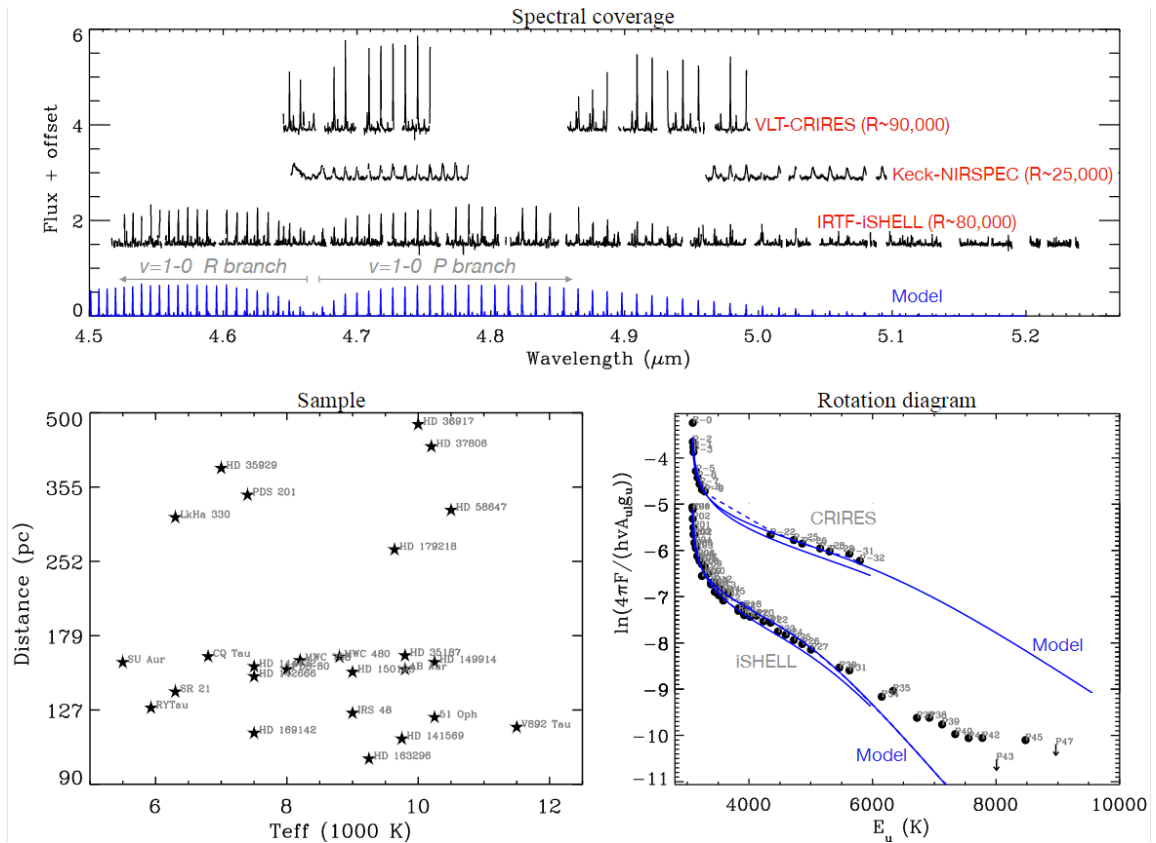


Figure 13. Spectral coverage comparison, preliminary sample, and rotation diagram comparison of instrument coverage. Top: example of an iSHELL spectrum in this survey as compared to spectra previously obtained with VLT-CRIRES and Keck-NIRSPEC. Bottom left: shows the variety of stellar temperatures and distances for a portion of the sample included in this survey. Bottom right: example of rotation diagrams for the ^{12}CO $v = 1 - 0$ lines for two different spectra observed with iSHELL and CRIRES. Observed emission lines or transitions are shown with black circles and black arrows indicate upper limits. Slab models with a single temperature and column density are superimposed shown in blue for reference (From Abernathy et al. 2021)

The unprecedented combination of large spectral coverage and high spectral resolution of iSHELL supports the collection of a homogenous overview of M-band CO spectra from protoplanetary disks. A portion of this sample was included in Banzatti et al. 2022 and combined with previous CRIRES data (see Figure 14). This sample includes a mix of T Tauris and Herbig stars, that span a wide range of properties, accretion rates, spectral

type, a variety of inclinations, and disks with and without inner dust cavities (see Figure 15).

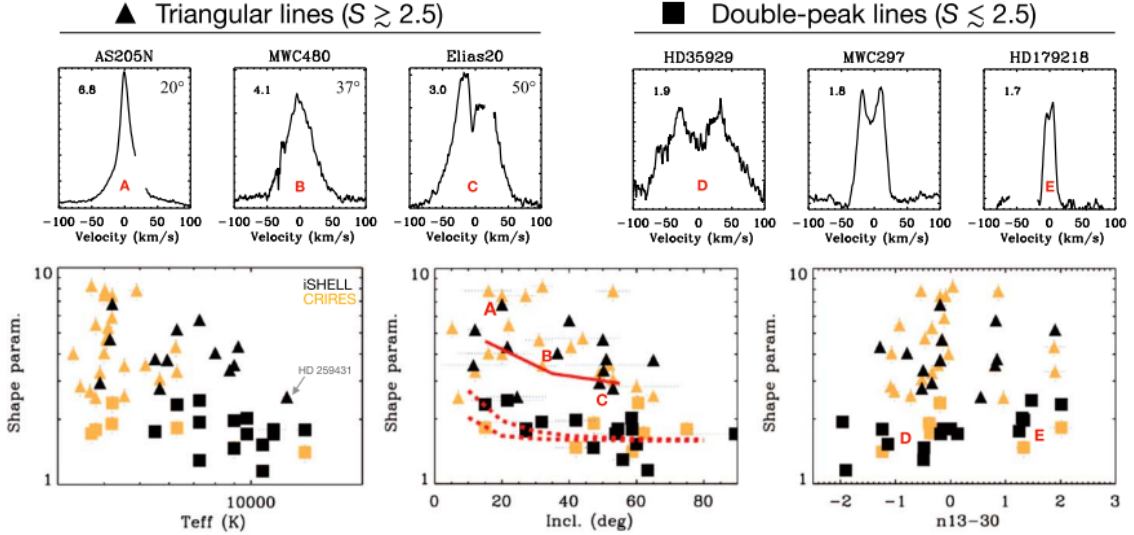


Figure 14. CO line shape parameter S as a function of T_{eff} , disk inclination, and infrared index. The symbols indicate the line shape parameter, with $S \geq 2.5$ categorized as triangular line profiles and $S \leq 2.5$ as double-peaked line profiles. The color indicates which instrument the data was taken with, black indicates iSHELL, and yellow indicates CRIRES. Top row: the two line profile categories, triangular and double-peaked, determined by S value. Bottom row: both line profiles are observed at all disk inclinations in disks with or without an inner cavity in T Tauri systems and Herbig AeBe disks. While triangular lines are more common in T Tauri systems and double-peaked more common in Herbig AeBe disks, as shown in the left plot (From Banzatti et al.2022).

Emission line profiles in this sample are separated into two groups: double peaked and triangular. These two line shapes are described using the line shape parameter S . This parameter uses the full line width at 10% and 75% of the peak flux, defining the line shape as $S = FW_{10\%}/FW_{75\%}$. This parameter is larger for triangular line shapes and smaller for double peaked line profiles with steep wings shown in the top panel of Figure 10. A gallery of most emission line profiles in this sample are shown in Figure 16.

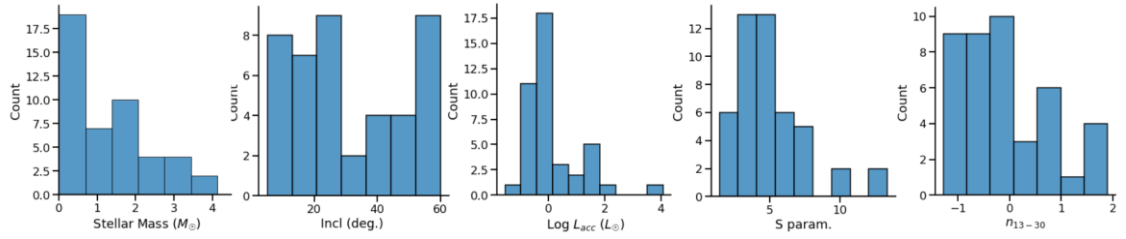


Figure 15. Histograms showing stellar and disk sample properties. Properties include: stellar mass, disk inclination, accretion luminosity, shape parameter, and infrared index. This is a portion of our 64 protoplanetary disks in our sample due to the measurements are not available for all objects.

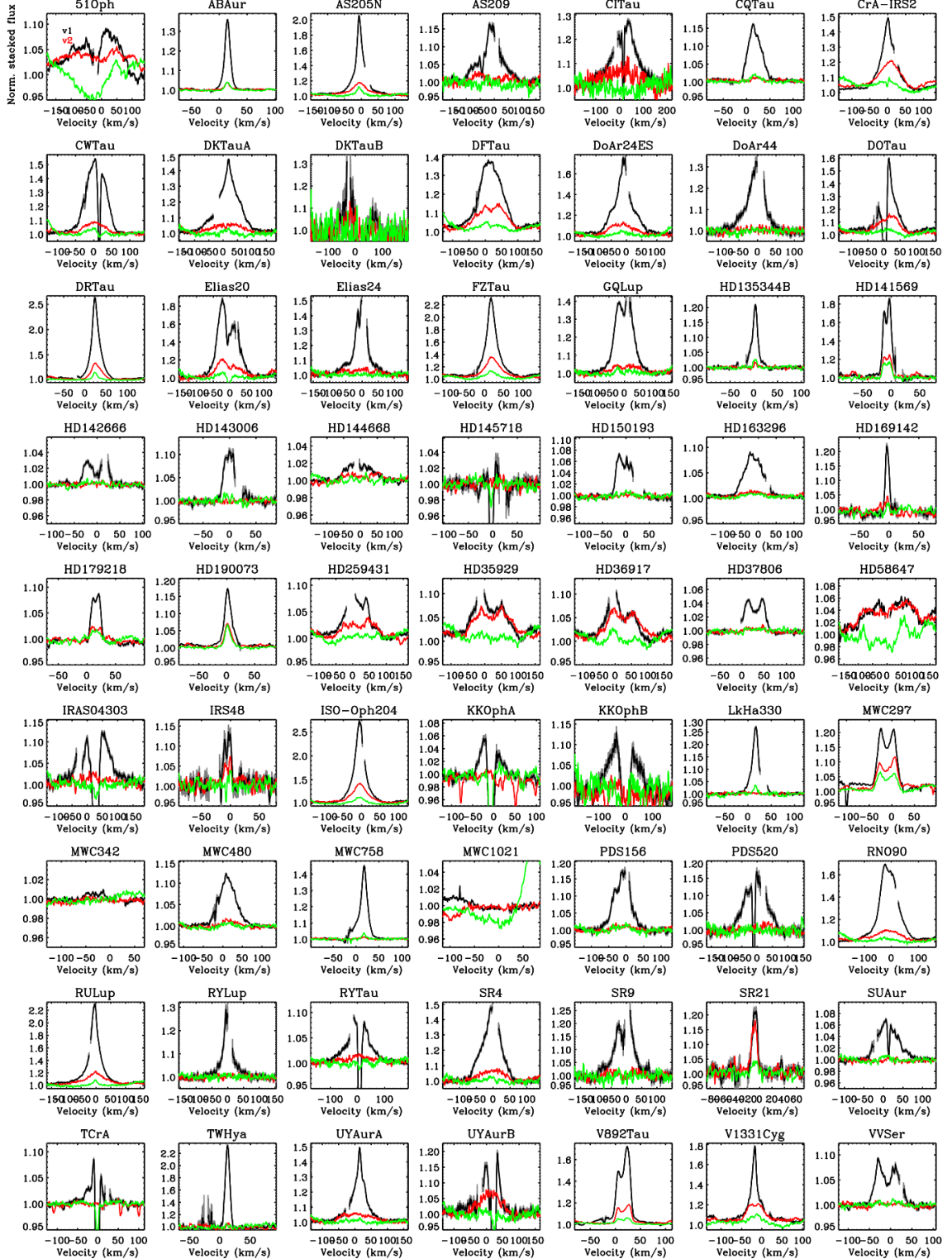


Figure 16. Overview of line profiles observed in this iSHELL survey. $^{12}\text{CO } v = 1 - 0$ is shown in black, $^{12}\text{CO } v = 2 - 1$ in red, and $^{13}\text{CO } v = 1 - 0$ in green. Stacked profile of Wa Oph 6 has been excluded.

II.II Data Reduction

In this section I will describe the reduction procedure and process using Spextool v5.0.3 (Cushing et al. 2004), an IDL-based package that can reduce iSHELL data, to create analysis-ready spectra. The purpose is both to describe each step and to provide a short guide in data reduction for future students. I will summarize the following steps of the reduction process and how these steps are implemented using Spextools (tool names given in parenthesis):

- Flat Fielding: create normalized images (xspextool)
- Wavelength Calibration (xspextool)
- Spectral Extraction: Apply nonlinearity correction to raw data, flat fielding correction, pair subtraction of A and B images, identify aperture positions, trace spectra, background subtraction, extract spectra (xspextool)
- Combination: combine extracted multi-order spectra by weighted average (xcombspec)
- Telluric correction: Remove absorption from Earth's atmosphere from the spectra (xtellcor)

Prior to using the Spextool reduction pipeline the raw data must be placed into a folder, a folder needs to be created for calibration files, and a folder for the processed files.

II.II.I Flat Fielding

The detector and optics of the telescope introduce distortions and variations, such as bad pixels and fringing introduced by optical elements of the telescope that affect the pixels of the detector used for observations. If the detector was perfect, it would appear uniformly grey. Flats are taken when the shutter is closed and to increase the S/N ratio, several flat fielding exposures are taken during the calibration process (see Figure 17). Spextool handles the correction process by combining the flats and computing the median flux level that can then be applied to the spectrum to remove variations introduced by the detector.

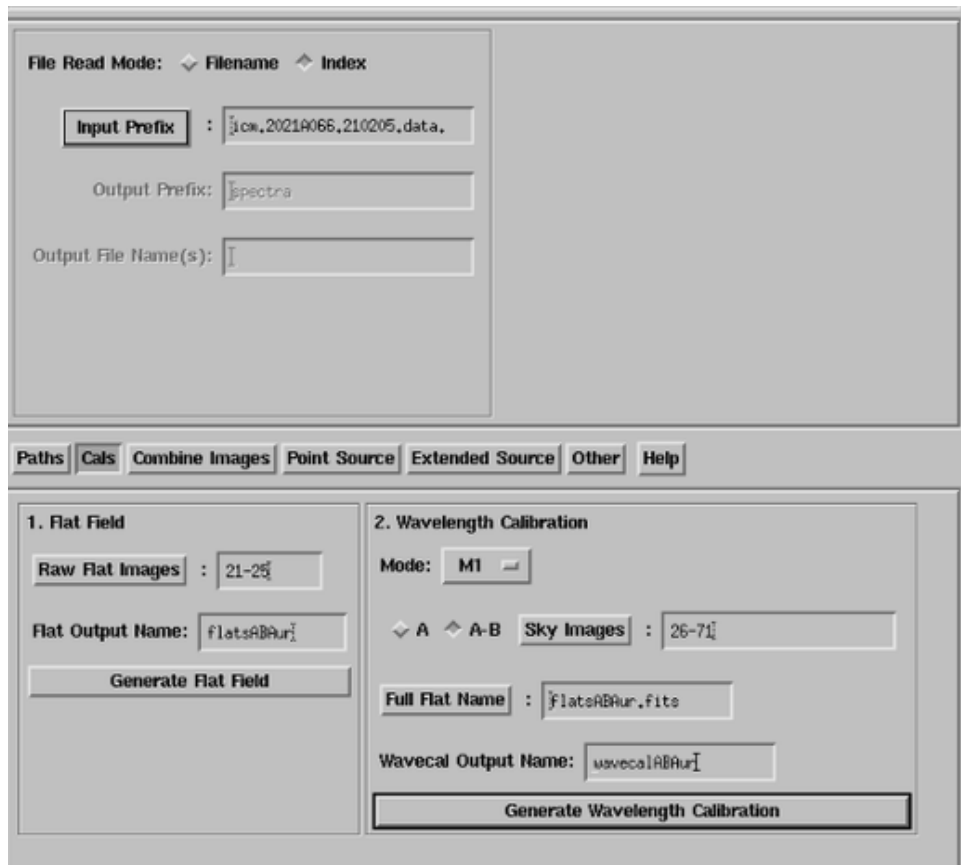


Figure 17. Xspextool calibration window for generating flat fields and wavelength calibration.

Flat fielding steps in xspextool:

- On the Cals tab set the input prefix for flats
- Enter the flat image numbers, output file name, and generate the flat field

An image of the detector will then appear that shows the different orders.

II.II.I Wavelength Calibration

The detector records data in terms of spatial direction, the orders of the spectra, and spectral direction, the pixels of the detector. Wavelengths must be assigned to each pixel of the detector before the spectra is ready for extraction. To do this, a pair of A and B frames are used to produce a night sky emission image. Order 106 of the sky emission is then compared to order 106 of a model spectrum (see Figure 18). The two spectra are then shifted to align the emission lines of the two. This process assigns wavelengths to the pixels along the spectral direction. In this data set shifts range from fractions of a pixel to 2-3 pixels.

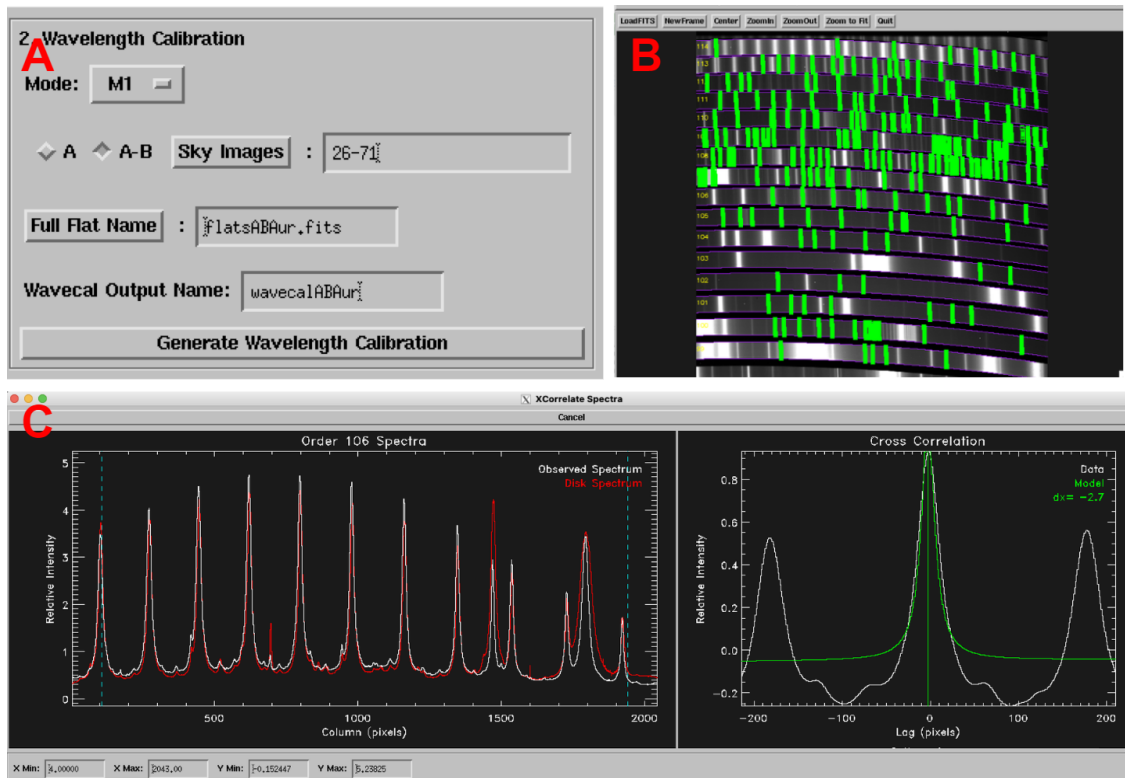


Figure 18. Xspextool wavelength calibration. A shows the user input window, B shows the sky line identification process that applies wavelengths to each pixel. Panel C shows the window that opens for finding an appropriate shift for the generated spectra (shown in red) compared to an observed spectra (shown in white).

Wavelength calibration steps in xspextool:

- Change the input prefix to data
- Select the mode that was used for the observations and the A-B setting.
- Enter the file number range of files for the target
- Generate the wavelength calibration
- Hit ‘S’ to select a range of a single emission line
- Repeat this step two times using other emission lines, avoiding the lines on the edge of the order

- If the dx value is fairly consistent, accept the shift.

II.II.III Spectral Extraction

To increase the signal-to-noise ratio, targets are observed over a period of time. This involves taking multiple detector images during the integration period for each target. To remove the background sky emission, we use the nodding methods, where two sky images, A and B, are taken with the target at different positions within the slit. One of these images is then subtracted from the other to isolate the science target (see Figures 19 and 20).

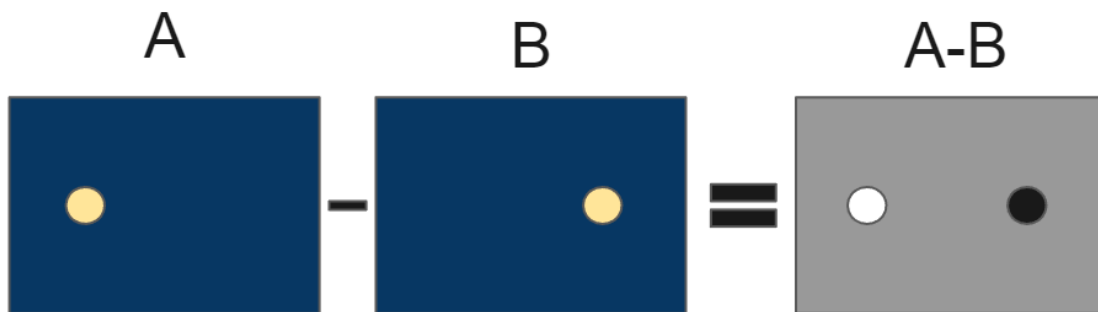


Figure 19. Example of the AB observing method used to isolate the science target and remove background emission.

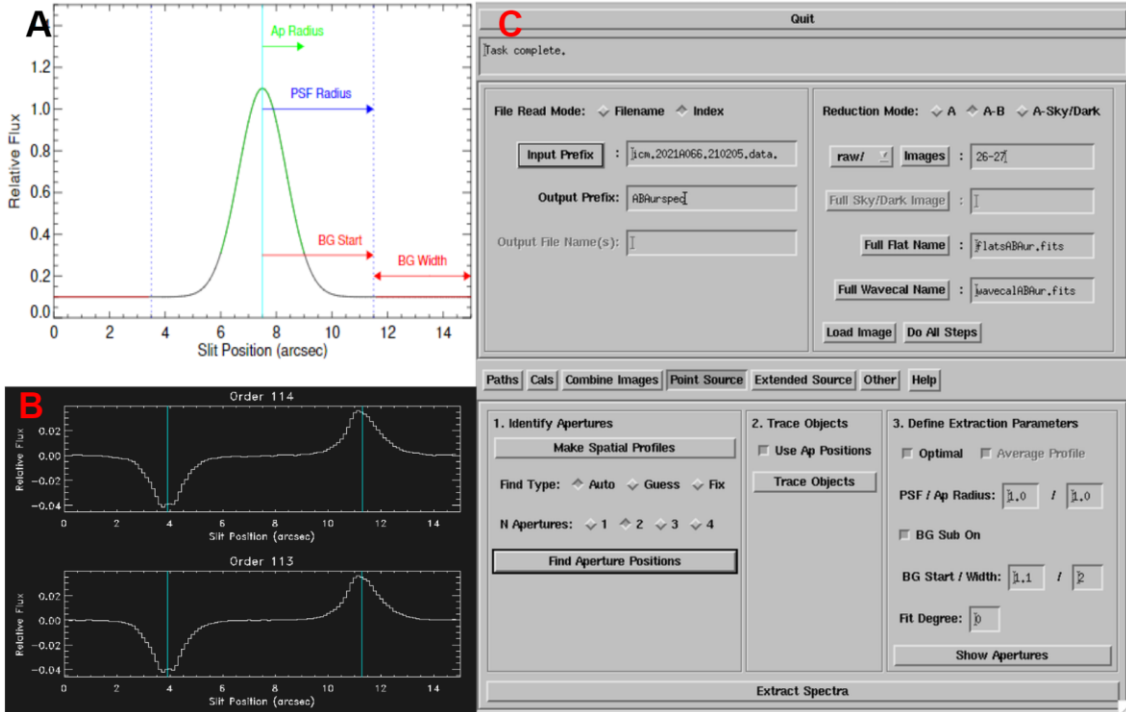


Figure 20. Xspextool point source spectral extraction window. A: shows the different user inputs (AP radius, PSF radius, BG start, and BG width) for fitting the spatial profiles. B: illustrates the spatial profiles obtained by viewing from the z-axis with the aperture positions defined and shown in blue. C: user setup interface, where calibration files are loaded, aperture positions are defined, and values entered to fit the spatial profiles.

This process produces two lines, a positive and a negative, for the spectra (Figure 16 panel B). To convert relative intensity into flux, these lines are viewed from the side or z-axis (add image to show the side view compared to spatial profiles) as spatial profiles. The shape of spatial profiles varies due to optical effects and atmospheric effects (Figure 21). User inputs for PSF/AP radius and BG start/width define the regions where there is flux and where the background is, shown in panel A of Figure 20. These parameters assist the pipeline with constructing an average profile for each pixel as an empirical fit to the z-axis. For each AB pair the shape is collapsed along the z-axis to give a flux for each wavelength.

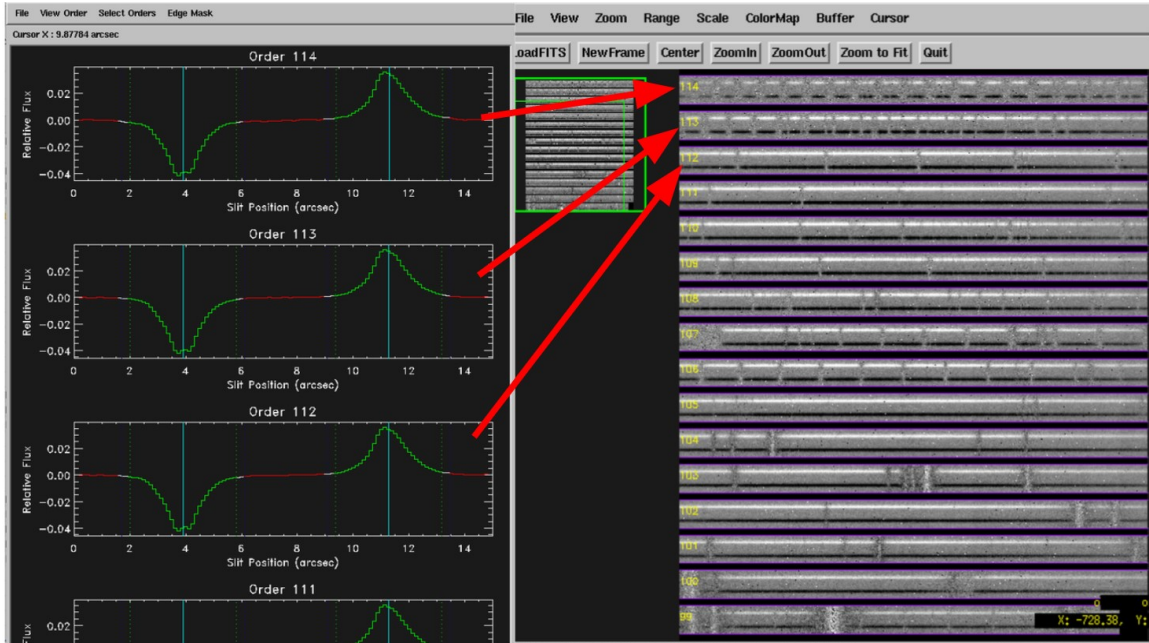


Figure 21. Xspextool point source extraction fitting the spatial profiles by order. Each profile on the left corresponds with an order shown on the detector. These profiles vary in shape depending on observation conditions.

Point source extraction steps in xspextool:

- Input the name of the flats and wavelength calibration files on the point source tab
- Input numbers of the first A B pair
- Select load image
- Select make spatial profiles
- Set find type to guess and apertures to two
- Select find apertures
- Select trace objects

- Input values for PSF/ AP radius and BG start/ width. Adjust these values until all of the emission is between the green lines for each peak

II.II.IV Combining Spectra

To increase the signal to noise ratio targets are observed for a period of time, obtaining multiple spectra that are then combined (see Figure 22). This is done by first scaling the spectra to the same flux, the pipeline measures the scaling factor for one order and applies it to all other orders. Then the individual spectra are stacked with the weighted average.

Combination steps in xcombspec:

- Set the input prefix
- Insert file numbers
- Select order 110, select a region without absorption features, and scale the spectra

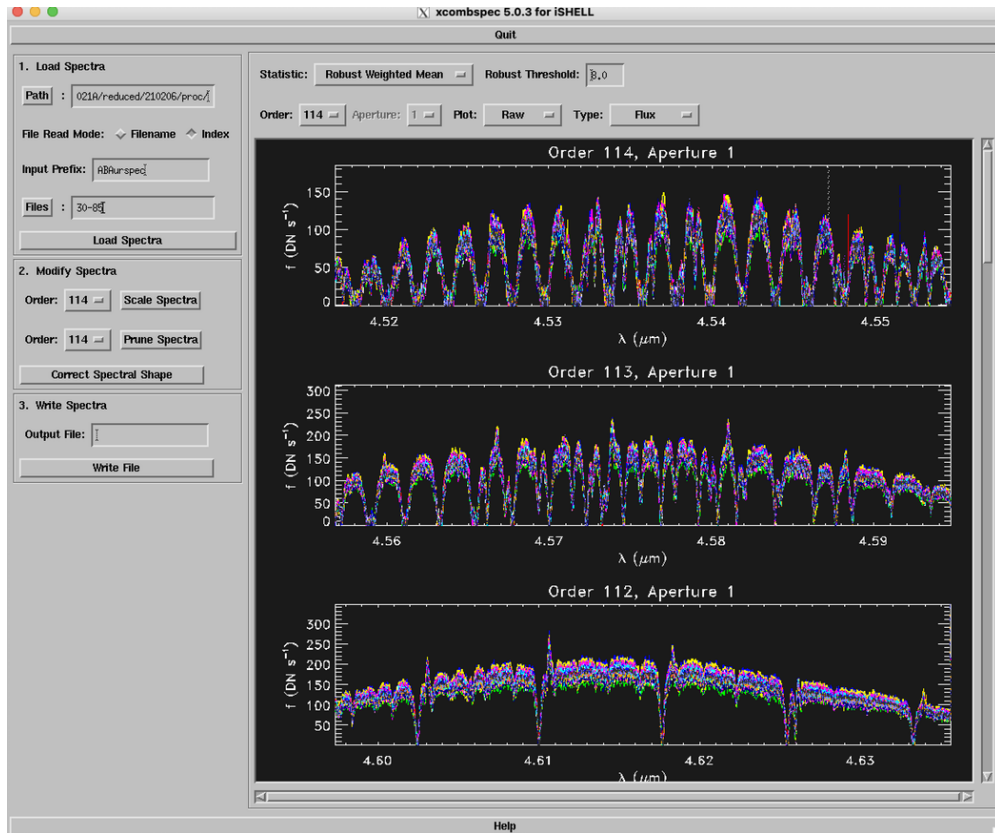


Figure 22. Xcombspec interface, each image taken during the observation is shown in a different color.

II.II.V Telluric Correction

In the IR range of the electromagnetic spectrum, absorption lines are strong due to H₂O, CO₂, CH₄, N₂O, O₂, and O₃ in the atmosphere. To correct for these telluric features, observations of a standard star, with a known spectral type and effective temperature, in the same region of the sky as the science target is needed. By knowing the spectral type and effective temperature of the standard, we know what the spectra should look like and can then determine the needed corrections to remove telluric features (see Figure 23). Spectra for the standard star should be processed the same as the science target. Similar to the wavelength extraction process, we shift the combined spectra of the target and standard star to best remove the telluric residuals.

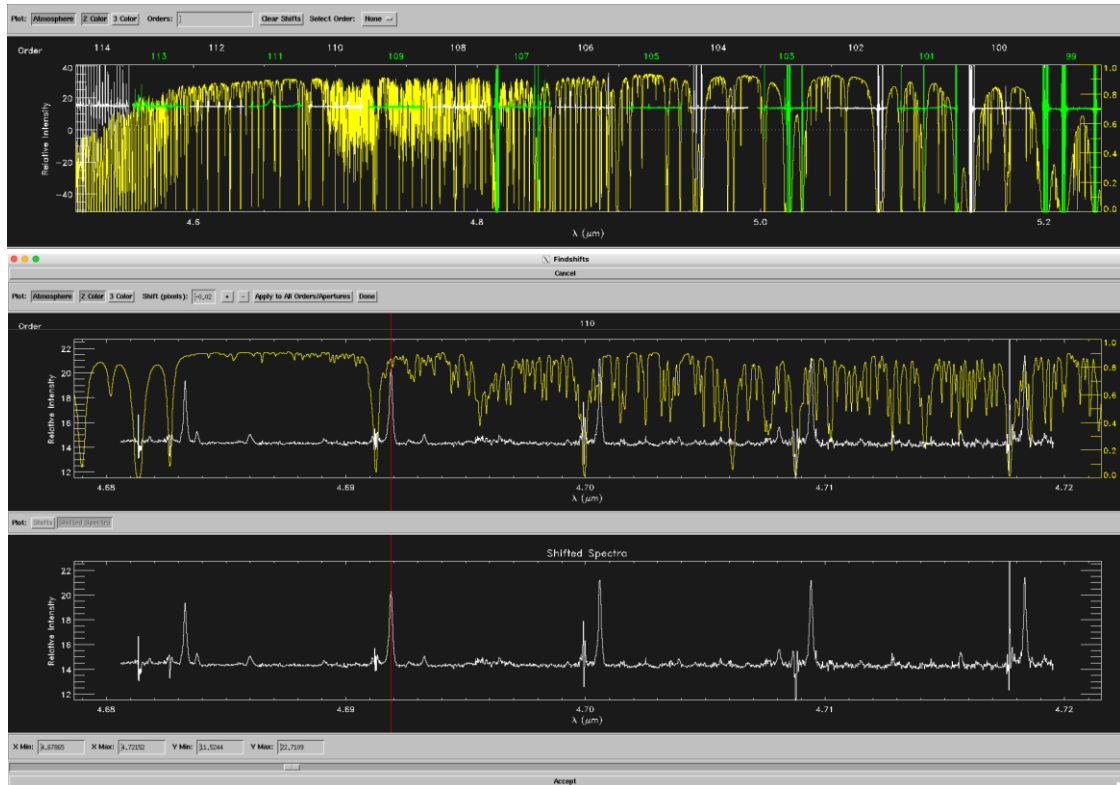


Figure 23. Xtellcorr window. This window shows the telluric features in yellow and the observed science target spectra in white.

Telluric correction steps in xtellcorr:

- Load standard star and target spectra
- Enter V-mag and surface temperature of standard star
- Select construct spectra and note the air mass of each spectra
- Select get shifts
- Select order 112
- Hit "s" and select a relatively flat section of the spectra to get shifts starting with order 112, apply the shift to all orders, and check shifts for other orders (111, 110, 105)
- Once an average shift has been determined, accept the shift

III. SLAB MODEL AND FITTING PROCEDURE

In the following sections I will describe the simple slab model used to fit our data and results are visualized using rotation diagrams. The decomposition of emission lines into components will also be described.

III.I Slab Model

A single-slab model is used to estimate the properties of CO spectra from the observations; the model includes 3 parameters: the excitation temperature T , the column density N , and the emitting area $A (= \pi R^2)$. This single-slab model, as described in Banzatti et al. 2012, assumes local thermodynamic equilibrium (LTE) and accounts for optical depth. Integrated line fluxes, line widths, and their uncertainties are loaded into the model as a guide for the model to produce a synthetic spectra comparable to our observed spectra. Einstein A-coefficients and statistical weights corresponding to the ro-vibrational transitions are taken from the high-resolution transmission molecular absorption (HITRAN) database. A chi-squared test is done to determine how well the model spectra compares to the loaded spectra. In order to find the absolute best fit the reduced chi-squared, $\tilde{\chi}^2$, is used. This is found by dividing χ^2 by the degrees of freedom, which is the difference between the number of line flux measurements and the free parameters: T , N , and R . The model explores a grid of T , N , and R to find the best fitting parameters, minimizing the $\tilde{\chi}^2$ value. The model then generates synthetic CO spectra as well as the best fit line fluxes. This is done for the $^{12}\text{CO } v = 1 - 0$, $^{12}\text{CO } v = 2 - 1$ that is sensitive to vibrational excitation, and $^{13}\text{CO } v = 1 - 0$ that is more sensitive to column density.

III.II Rotation Diagrams

The rotation/population diagram technique has been described in detail in Goldsmith & Langer 1999 and is used to visualize the data and best fit model from the slab model. This technique can clearly show temperature and opacity effects (Figure 24) as well as deviations from the single slab in LTE approximation. Rotation diagrams, also referred to as population diagrams, visually represent physical properties that cause molecular gas to become excited and give rise to emission lines. In this work, we use the formalism as in Larsson et al. 2002 (their equation 1):

$$\ln\left(\frac{4\pi F}{h\nu g_u A_{ul}}\right) = \ln\left(\frac{N}{Q(T)}\right) - \frac{E_{up}}{kT},$$

Where F is the integrated line fluxes of emission lines from a spectrum, their rest wavelength, the Einstein, A_{ul} coefficient of spontaneous emission for the upper and lower energy levels, statistical weight, g_u , frequency of the transition, ν , Planck's constant, h , and $Q(T)$ is a function of excitation temperature. The x-axis is the upper-level energy, E_u , which we adopt in units of Kelvin, implying that we divide E_{up} in erg by the Boltzmann constant, k_B , in erg/K, as:

$$E_u(K) = \frac{E_{up}}{k_B}.$$

Under LTE conditions, rotation diagrams can estimate temperatures and column density if CO is optically thin, and the energy levels are thermally populated. Which means the excitation is proportional to the slope of the rotation diagram, and the column density can be assumed to be the column density of the entire species of molecule. An increasingly steeper slope indicates a higher temperature and increasing curvature indicates a higher column density, as shown in Figure 24. As the temperature increases while at a fixed column density, the different levels become more populated. While when

the temperature is held constant, curvature appears as the gas becomes more optically thick. As gas becomes optically thick it is harder to use the slope as an indicator of temperature.

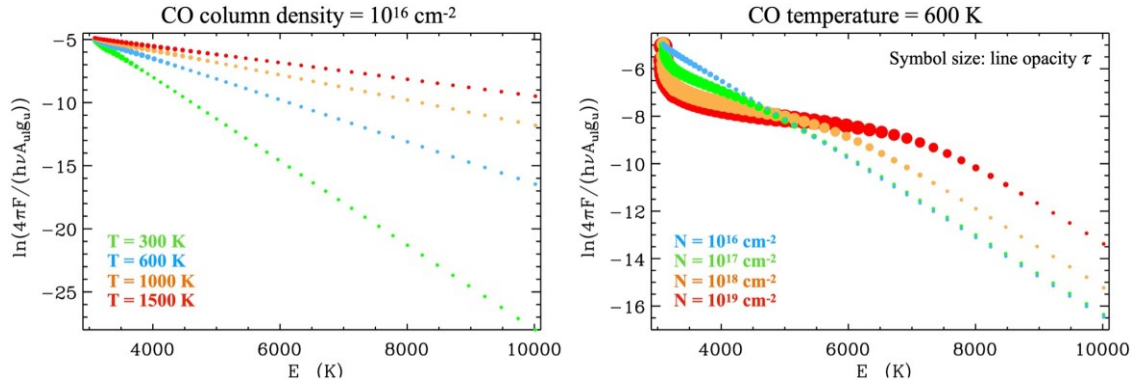


Figure 24. Example of the rotation diagram technique applied to a model $^{12}\text{CO } \nu = 1 - 0$ spectra. Each data point is an emission line from models where T and N are varied as shown in the legend. Left: the column density is fixed, and temperature is varied. Right: the temperature is fixed and the column density varies. The emitting area in each model is adjusted for visualization purposes so that they overlap in the top left corner of the diagram (the stronger low- J lines).

To test the reliability of slab model results for fit using more incomplete spectral coverage (see top panel of Figure 13), as in CRILES and NIRSPEC data, different portions of one spectra were fitted using the simple slab model for a single disk. This produces very different results (see Figure 25) for column density and temperature while attempting to match the observed spectra, suggesting caution when fitting and interpreting previously obtained CO spectra with more incomplete spectral coverage (see Figure 26). With iSHELL observations a more complete rotation diagram better reflects the combination of column density, temperature, and excitation.

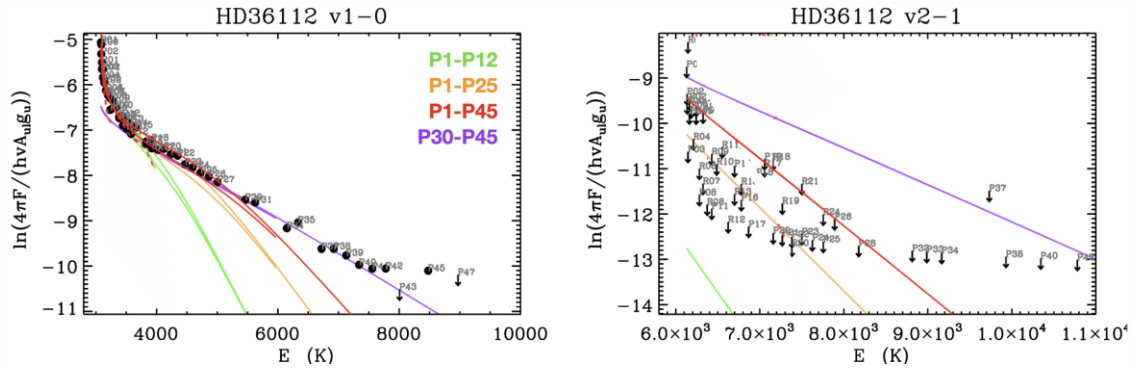


Figure 25. The rotation diagram technique applied to different ranges of $^{12}\text{CO } \nu = 1 - 0$ lines. Black circles are emission lines or transitions from the observed spectra, while black arrows are upper limits. Color coding of the models indicates the portion of the spectra used to generate the fit as listed in the legend. Left: results from slab model used to reproduce $\nu = 1 - 0$ rotation diagram. Right: results from slab model used to produce $\nu = 2 - 1$ rotation diagram.

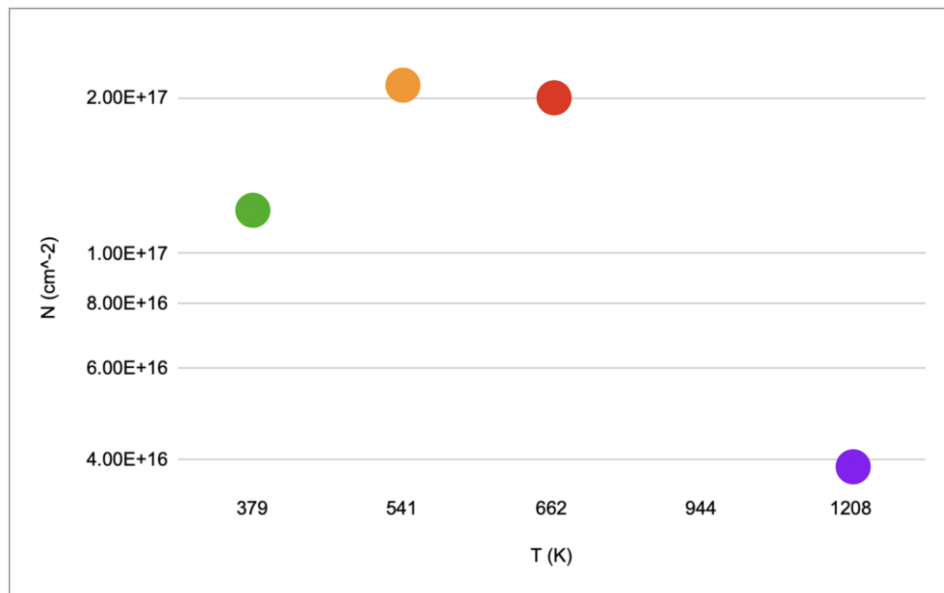


Figure 26. Best-fit model results for Figure 25. Colors correspond to the different portions of spectra fit with the slab model as listed on the legend of Figure 25.

III.III Line Decomposition

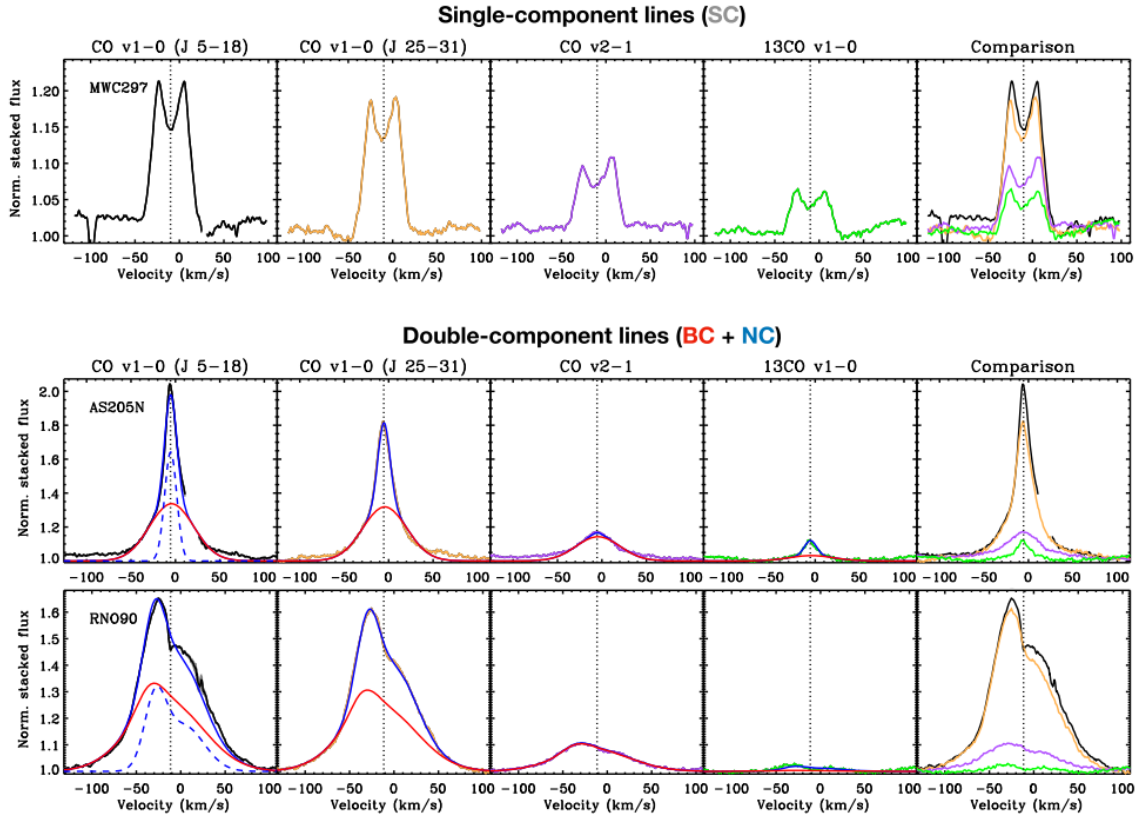


Figure 27. Examples of the stacked line profiles and decomposition into a broad component (BC) and narrow component (NC) where present. The dotted vertical line indicates the line center for reference. Top: example of a spectrum with a double-peaked line profile fit as a single component (SC). Middle and bottom: two examples of triangular lines fit using two components, BC marked in red, and NC marked in blue. Dotted blue line shows NC by itself (From Banzatti et al. 2022)

To best describe the line profiles, stacked lines were used to identify line components for each object in our sample. A portion of the line profiles within our sample can be described using a single component (SC). Other stacked line profiles are best described using a broad component (BC) to fit the wings and a narrow component (NC) that describes the emission at the center of the line (Figure 27). Each of these components have different FWHM that indicate the emission is from different regions in

the disk. Fluxes for each component are extracted, input into the slab model, and fit separately.

IV. RESULTS AND DISCUSSION

As a part of our systematic rotation diagram analysis of our sample, we have leveraged the unprecedented coverage of iSHELL to explore CO excitation in different types of lines and components. The rotation diagram for the BC of AS 205 N (Figure 28) shows how our simple slab model in LTE yields a best fit that reproduces the curvature in the rotation diagram of $\nu = 1 - 0$ lines.

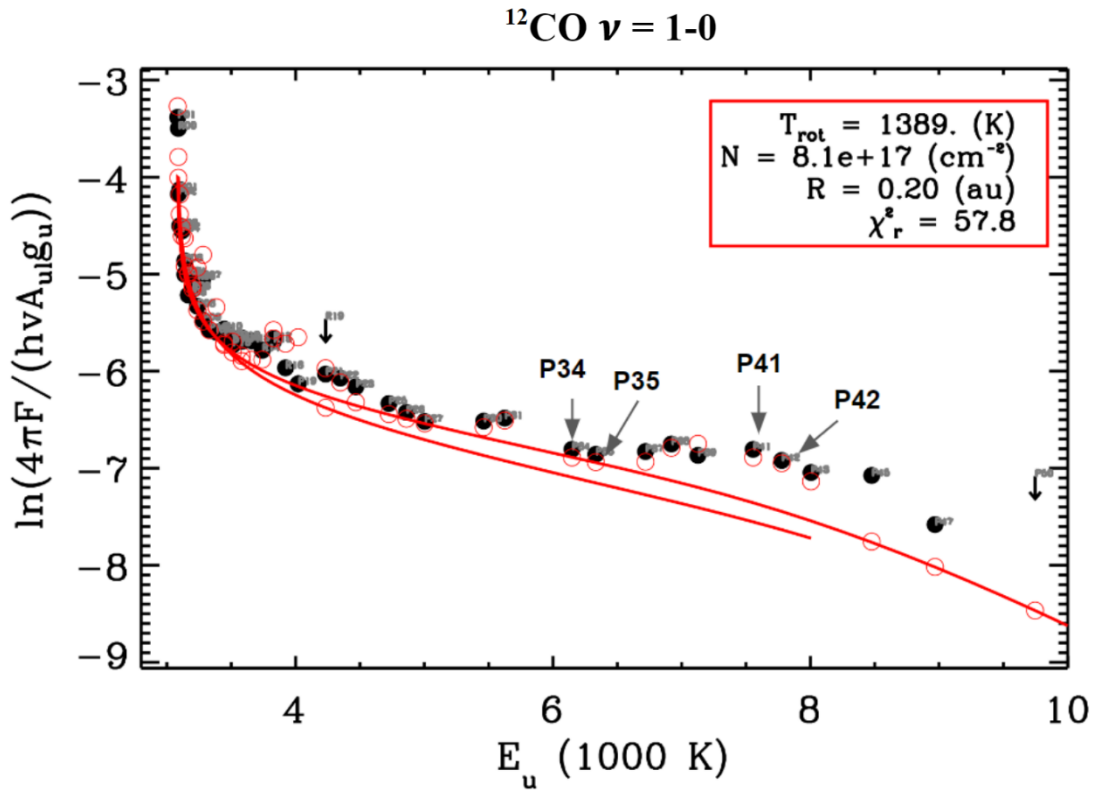


Figure 28. Slab model fit for AS 205 N BC with the best fitting model results reported. Each data point shown in black is an emission line from the observed spectra and black arrows are upper limits. The red solid line represents the model without considering blending between lines. Red open circles represent the model considering blending between lines. As a gap forms between the two versions of the model, it indicates blending of lines.

This rotation diagram illustrates the differences between a model that considers the blending of $\nu = 1 - 0$ lines with $\nu = 2 - 1$ lines (open circles in Figure 28) and a model that only considers the $\nu = 1 - 0$ lines (solid line in Figure 28). When looking at the spectra for AS 205 N (Figure 29) P33, P34, and P35 are spaced far enough from the $\nu = 2 - 1$ and show no blending. This is reflected by the two models and data matching well in Figure 28. P41, P42, and P43 show clear blending with $\nu = 2 - 1$ lines, which is reflected by the underprediction of the model that does not consider blending.

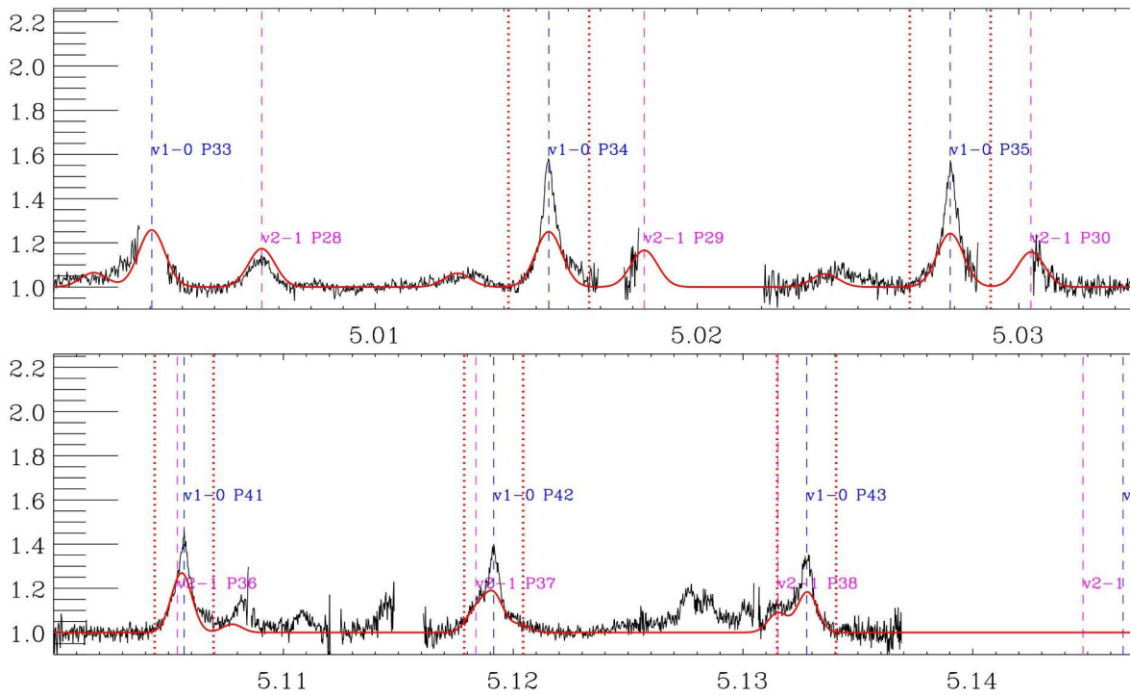


Figure 29. Two segments of the spectra observed for AS 205 N. The vertical dashed blue lines to show the line center of $^{12}\text{CO } \nu = 1 - 0$ lines and dashed pink lines to show the center of $^{12}\text{CO } \nu = 2 - 1$ lines. The black line is the observed spectra, while the red shows the broad component model. The top row shows how the P33, P34, and P35 $^{12}\text{CO } \nu = 1 - 0$ lines are not blended with the $^{12}\text{CO } \nu = 2 - 1$ lines. The bottom row shows the P41, P42, and P43 $^{12}\text{CO } \nu = 1 - 0$ lines and $^{12}\text{CO } \nu = 2 - 1$ lines blending together.

An empirical analysis of a portion of the sample included in this work presented in Banzatti et al. 2022 systematically collected line ratios to provide an overview of

diverse excitation conditions and trends. Measured properties and excitation of observed CO were combined to describe the regions and conditions where different line types and velocity components may trace in disks, see Figure 30. ^{12}CO excitation was studied through three line ratios: high-J (J levels between 25 and 31) to low-J (J levels between 5 and 18) ratios of $v = 1 - 0$ (proxy for rotational temperature), $v = 2 - 1$ (v_2) to $v = 1 - 0$ (v_1) (proxy for vibrational excitation), and $^{12}\text{CO}/^{13}\text{CO}$ (proxy for column density). The top panel of Figure 30 shows a broad trend for each of the three ratios increasing as a function of CO FWHM. The ratio of high-J to low-J shows BC having the highest rotational excitation. While the ratio of v_2/v_1 shows a more complex behavior where the ratio increases as a function of FWHM, we see broad groupings of components. The bottom panel of Figure 30 shows broad trends in inclination, where the inclination is increasing as CO FWHM increases, which is due to viewing effects. While the infrared index, n_{13-30} , shows the opening of a gap within the disk. These three excitation tracers do not show noticeable trends with stellar mass and accretion luminosity.

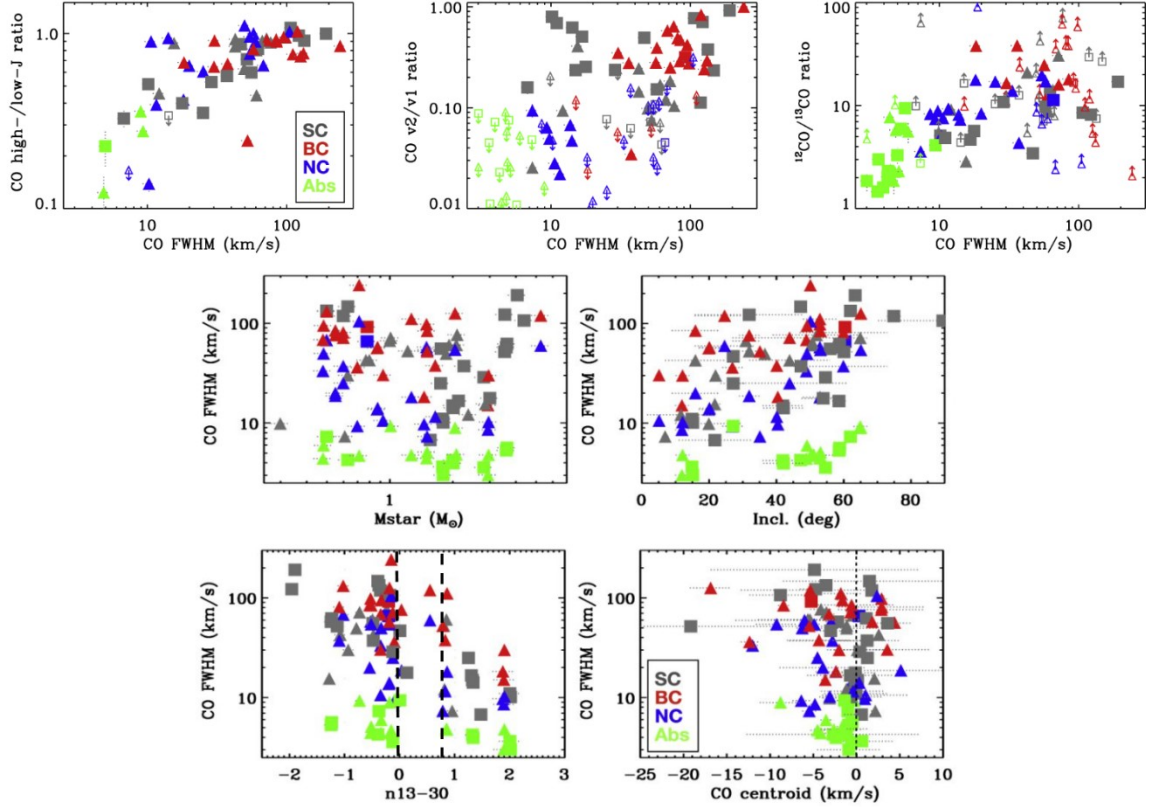


Figure 30. CO kinematics for various components. SC (grey), BC (red), NC (blue), and absorption (green) from combined the iSHELL and CRIRES surveys. Symbols reflect the shape parameter S , where double-peaked lines are marked with squares and triangular lines with triangles (From Banzatti et al. 2022).

In this thesis, we build on the line flux ratios presented in Banzatti et al. 2022 and replace these ratios with temperature and column density outputs from the slab model for the $^{12}\text{CO } v = 1 - 0$ band, $^{12}\text{CO } v = 2 - 1$ band, and $^{13}\text{CO } v = 1 - 0$. Slab model results for $^{12}\text{CO } v = 1 - 0$, $^{12}\text{CO } v = 2 - 1$, $^{12}\text{CO } v = 1 - 0$ combined with $^{12}\text{CO } v = 2 - 1$, and $^{13}\text{CO } v = 1 - 0$ are reported in Tables 2-5 shown below. The emitting radius is reported as R norm., where the normalization is on the spectrum such that R is the equivalent area emitting radius for the spectrum normalized to a continuum of 1 (ie. not flux calibrated).

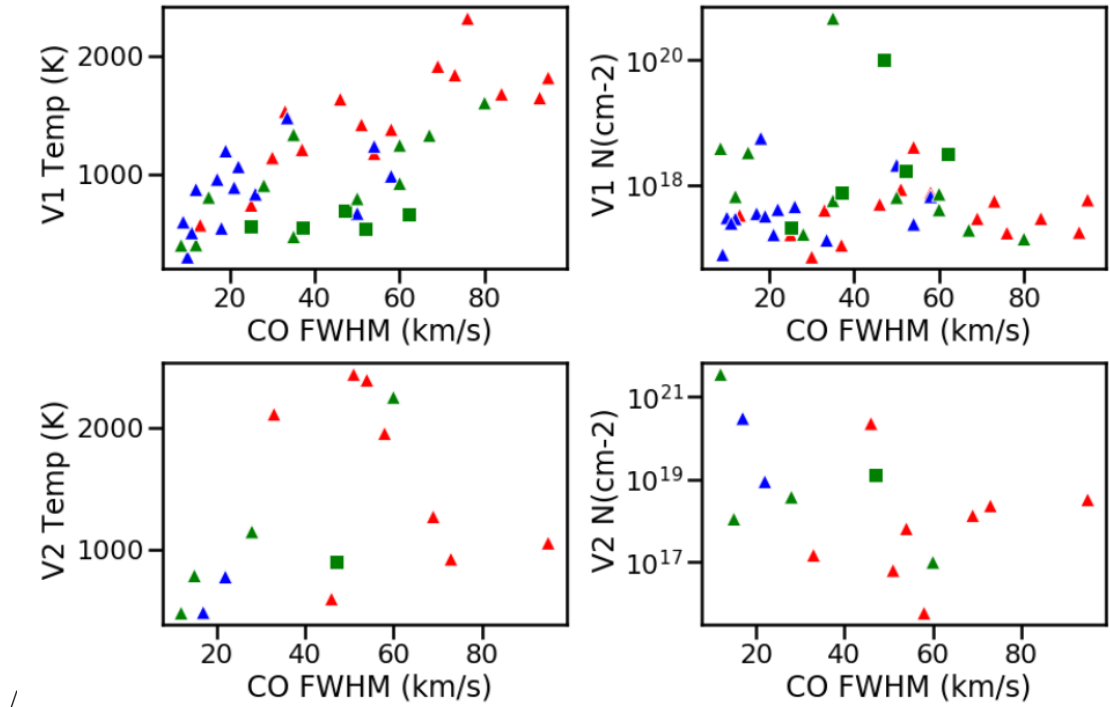


Figure 31. ^{12}CO fit results for $v = 1 - 0$ (V1) and $v = 2 - 1$ (V2) temperature and column density compared to CO FWHM. The two emission categories determined by the shape parameter, S , are denoted with squares and triangles for double-peaked and triangular lines respectively. The line components are denoted by color: NC (blue), BC (red), SC (green).

When compared to trends seen when analyzing line ratios used as proxies for excitation and column density in Banzatti et al. 2022, the ^{12}CO $v = 1 - 0$ temperature, T , results (Figure 31) show a similar dependence on line width regardless of component and line profile type. The range of line widths probed reflect different radii within the disk, showing a correlation to the region within the disk and the rotational excitation. Our results also show BC, such as AS 205 N, having the highest rotational excitation, and NC overall having lower rotational excitation, as shown by the ^{12}CO high-J to low-J ratio in Figure 30. However, the column density plot is relatively flat overall in comparison to the positive trend shown by $^{12}\text{CO}/^{13}\text{CO}$ in Figure 25. The ^{12}CO $v = 2 - 1$ results, instead are

rather sparse and hard to determine any overall trends, showing a need for more spectra with detection of $\nu = 2 - 1$ emission.

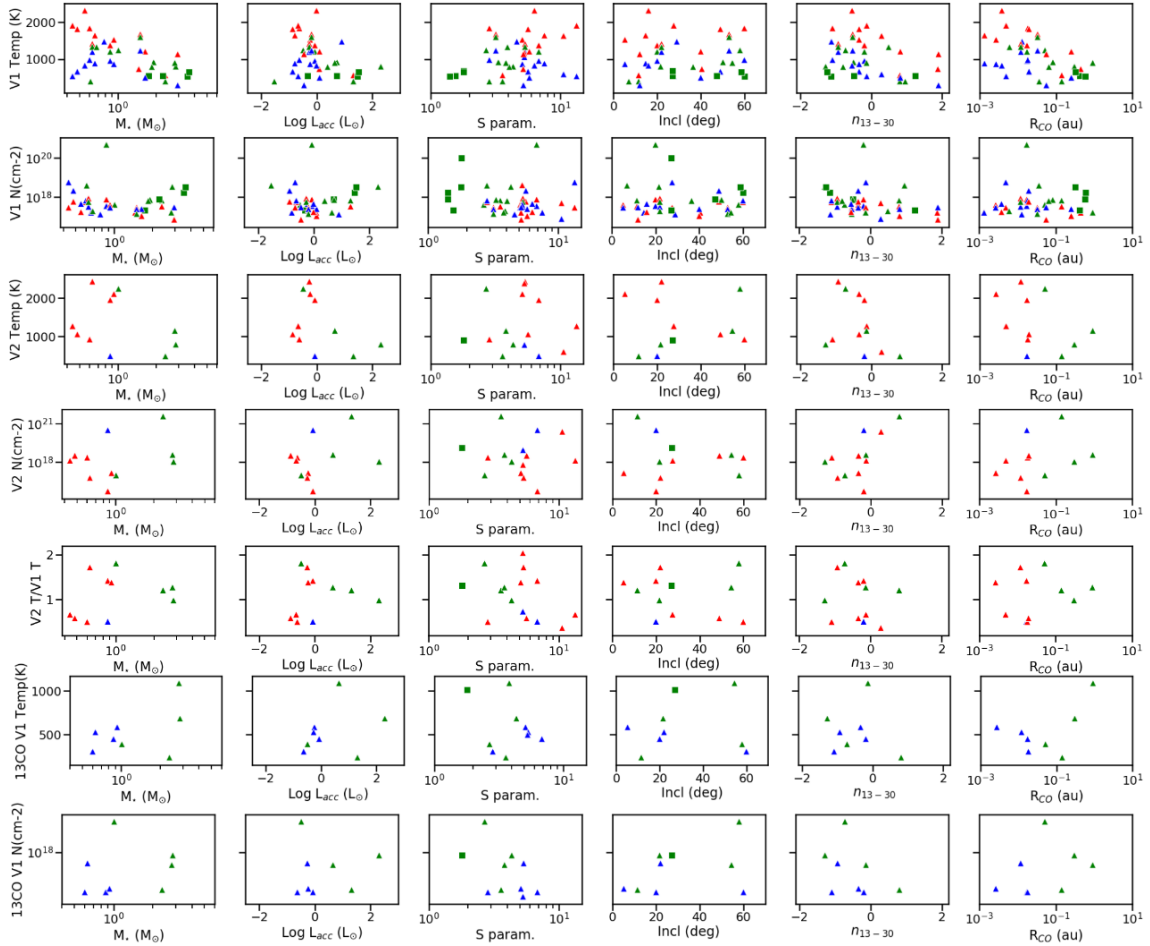


Figure 32. Slab model results for $^{12}\text{CO } \nu = 1 - 0$, $^{12}\text{CO } \nu = 2 - 1$, and $^{13}\text{CO } \nu = 1 - 0$. The colors reflect the different components as described in Figure 31 compared to stellar mass, accretion luminosity, shape parameter, disk inclination, infrared index, and the characteristic emitting radius of CO.

A broader collection of correlations between slab model results and system parameters related to stellar and accretion properties, and disk structure and viewing angle is shown in Figure 32. A trend we identify for the $\nu = 1 - 0$ emission is overall lower ^{12}CO temperatures for disks with higher mass stars. This seems counter-intuitive since more massive stars have a higher temperature, and the CO should be hotter. One

interpretation is that the CO is at larger radii in more massive stars therefore the CO is colder. This interpretation is supported by the plot with R_{CO} , where the hotter CO is closer while colder CO is at a further radius. The n_{13-30} shows a similar trend, where as dust is depleted CO moves to larger radii, and therefore is cooler. In Banzatti et al. 2022, it is suggested that mixing with dust could suppress the vibrational temperature by limiting the visible column of hot gas.

The $v = 1 - 0$ column density for ^{12}CO shows several trends with the stellar and disk properties. The first being a correlation between column density decreasing and larger n_{13-30} values, which can be interpreted as gas depletion happening as dust is depleted. We also see a peculiar trend with stellar mass that decreases roughly up to $M_{Star} \approx 1 M_{\odot}$, and then increases. This trend is also seen in the plot with L_{acc} , where there is a decrease until $\text{Log } L_{acc}/L_{\odot} \approx 0 L_{\odot}$, and then increases. These two unexpected trends with stellar mass and accretion luminosity were not observed in Banzatti et al. 2022, where there were no noticeable trends. There are no obvious trends within the ^{12}CO $v = 1 - 0$ or ^{13}CO plots, more spectra with ^{12}CO $v = 1 - 0$ and ^{13}CO detections are needed for a more complete analysis.

Table 2. ^{12}CO $v = 1 - 0$ slab model fit results.

Name	Comp	FWHM (km/s)	V1 T (K)	V1 N (cm^{-2})	R norm. (AU)	chi2_red
AB Aur	SC	12	398	6.48E+17	1.8	43.2
AB Aur	BC	13	565	3.23E+17	0.6	15.5
AS205N	BC	58	1389	8.1E+17	0.2	57.8
AS205N	NC	17	954	3.45E+17	0.3	17
AS205N	SC	35	1203	4.38E+17	0.3	121.8
CW Tau	SC	60	1243	3.98E+17	0.4	55.2

Name	Comp	FWHM (km/s)	V1 T (K)	V1 N (cm ⁻²)	R norm. (AU)	chi2_red
DFTau	BC	73	1841	5.46E+17	0.2	135.9
DFTau	NC	58	981	6.47E+17	0.3	28.2
DKTauA	BC	93	1646	1.72E+17	0.3	40.5
DKTauA	NC	21	884	1.58E+17	0.2	2.3
DOTau	BC	69	1914	2.86E+17	0.2	26.2
DOTau	NC	18	538	5.56E+18	0.6	14
DRTau	BC	33	1530	3.89E+17	0.3	155.5
DRTau	NC	12	868	2.84E+17	0.4	48
Elias20	BC	95	1817	5.72E+17	0.2	20.3
Elias20	NC	50	665	2.06E+18	0.8	11.3
Elias24	NC	33.5	1477	1.29E+17	0.3	4.7
FZTau	BC	51	1418	8.42E+17	0.3	91.4
FZTau	NC	19	1195	3.13E+17	0.2	66.4
FZTau	SC	35	1334	5.54E+17	0.4	140.9
HD143006	SC	25	554	2.08E+17	0.4	0.1
HD150193	SC	37	543	7.45E+17	0.5	0.5
HD163296	SC	60	919	7.08E+17	0.2	10.7
HD190073	SC	15	801	3.26E+18	0.2	19.8
HD37806	SC	52	539	1.68E+18	0.4	1.9
ISO-Oph204	BC	54	1173	4.00E+18	0.3	72.3
ISO-Oph204	NC	22	1061	4.01E+17	0.4	39
LkHa330	BC	30	1138	6.94E+16	0.2	1.9
LkHa330	NC	10	294	2.95E+17	4.4	1.7
MWC297	SC	47	685	1.00E+20	0.4	710.5
MWC480	SC	50	790	6.26E+17	0.3	6.9
MWC758	BC	37	1207	1.07E+17	0.2	7.3
MWC758	NC	11	500	2.42E+17	0.8	19.7
RNO90	BC	84	1679	2.88E+17	0.3	134.1
RNO90	NC	54	1234	2.33E+17	0.3	173.7

Name	Comp	FWHM (km/s)	V1 T (K)	V1 N (cm ⁻²)	R norm. (AU)	chi2_red
RNO90	SC	80	1603	1.35E+17	0.4	302.9
RULup	BC	76	2321	1.69E+17	0.2	30.4
RULup	NC	26	829	4.44E+17	0.5	12.6
SR4	SC	67	1327	1.87E+17	0.3	5.7
TWHya	SC	8.5	393	3.81E+18	2.5	7.3
V892Tau	SC	28	902	1.60E+17	0.5	127.1
V1331Cyg	BC	46	1635	4.85E+17	0.2	24
V1331Cyg	NC	9	592	7.55E+16	0.6	7.8
VVSer	SC	62	655	3.16E+18	0.3	10.3

Table 3. ¹²CO $v = 2 - 1$ slab model fit results.

Name	Comp	FWHM (km/s)	V2 T (K)	V2 N (cm ⁻²)	R norm. (AU)	chi2_red
AB Aur	SC	12	480	3.51E+21	0.3	4.2
AS205N	BC	58	1951	5.71E+15	0.7	57.8
AS205N	NC	17	484	3.02E+20	0.4	1.6
CW Tau	SC	60	2247	9.77E+16	0.2	5.8
DFTau	BC	73	921	2.29E+18	0.3	52.6
DOTau	BC	69	1269	1.32E+18	0.2	4.5
DRTau	BC	33	2109	1.45E+17	0.2	19.9
Elias20	BC	95	1054	3.22E+18	0.2	6
FZTau	BC	51	2435	6.18E+16	0.3	54.1
HD190073	SC	15	786	1.09E+18	0.1	16.3
ISO-Oph204	BC	54	2389	6.35E+17	0.1	85.9
ISO-Oph204	NC	22	776	8.78E+18	0.2	5.8
MWC297	SC	47	897	1.27E+19	0.2	988.6
V892Tau	SC	28	1146	3.72E+18	0.1	84.4
V1331Cyg	BC	46	595	2.28E+20	0.6	41.1

Table 4. ^{12}CO $v = 1 - 0$ and $v = 2 - 1$ slab model fit results.

Name	Comp	FWHM (km/s)	V1+V2 T (K)	V1+V2 N (cm^{-2})	R norm. (AU)	chi2_red
AB Aur	SC	12	459	5.88E+17	1.1	42.8
AB Aur	BC	13	606	3.32E+17	0.5	11.7
AS205N	BC	58	1324	3.07E+17	0.2	101.3
AS205N	NC	17	777	3.00E+17	0.5	40
CW Tau	SC	60	1011	2.23E+17	0.5	105.4
DFTau	BC	73	1479	5.33E+17	0.2	109.3
DFTau	NC	58	959	6.46E+17	0.3	16.4
DK TauA	BC	93	1353	1.22E+7	0.4	57.9
DK TauA	NC	21	869	1.55E+17	0.2	1.3
DOTau	BC	69	1672	2.39E+17	0.2	21.4
DRTau	BC	33	1273	2.26E+17	0.3	158.8
DRTau	NC	12	798	2.52E+17	0.4	28.9
Elias20	BC	95	1522	2.50E+17	0.3	34.1
Elias20	NC	50	611	2.55E+18	0.9	6.7
FZ Tau	BC	51	1376	3.49E+17	0.3	109
FZ Tau	NC	19	908	2.36E+17	0.4	54.3
HD143006	SC	25	554	2.08E+17	0.4	0.1
HD150193	SC	37	544	7.50E+17	0.4	0.3
HD163296	SC	60	918	4.40E+17	0.2	14.1
HD190073	SC	15	759	2.31E+17	0.2	32.2
HD37806	SC	52	533	1.72E+18	0.4	1

Name	Comp	FWHM (km/s)	V1+V2 T (K)	V1+V2 N (cm ⁻²)	R norm. (AU)	chi2_red
ISO-Oph204	BC	54	1319	9.99E+17	0.3	171.3
ISO-Oph204	NC	22	516	2.96E+18	1.5	69
LkHa330	BC	30	1097	7.29E+16	0.2	1.1
MWC297	SC	47	644	7.39E+19	0.4	1183.8
MWC480	SC	50	796	5.94E+17	0.3	4.3
MWC758	BC	37	1182	1.01E+17	0.2	4.2
MWC758	NC	11	501	2.43E+17	0.8	10.1
RNO90	BC	84	1542	9.37E+16	0.4	457.5
RNO90	NC	54	958	2.61E+17	0.4	184.8
V892Tau	SC	28	1040	2.12E+17	0.4	172.2
V1331Cyg	BC	46	1591	5.62E+17	0.2	33.4
VVSer	SC	62	632	2.58E+18	0.4	10.6

Table 5. ¹³CO $v = 1 - 0$ slab model fit results.

Name	Comp	FWHM (km/s)	¹³ CO T (K)	¹³ CO N (cm ⁻²)	R norm. (AU)	chi2_red
AB Aur	SC	12	235	8.86E+16	10.7	3.9
AS205N	NC	17	447	7.64E+16	0.8	4.3
CW Tau	SC	60	387	7.13E+18	1.5	3.6
DFTau	NC	58	303	7.63E+16	4	0.1
DRTau	NC	12	582	9.55E+16	0.4	4.7
FZ Tau	NC	19	525	4.89E+17	0.4	1.8
HD190073	SC	15	682	8.17E+17	0.2	5.3
ISO-Oph204	NC	22	494	5.73E+16	0.8	5.1
MWC297	SC	47	1011	8.11E+17	0.1	379.8
V892Tau	SC	28	1087	4.39E+17	0.1	43

V. CONCLUSION

In this work, we leveraged the unprecedented coverage and resolution obtained with IRTF-iSHELL as part of an ongoing M-band spectroscopic survey of protoplanetary disks. We systematically reduced spectra for 64 protoplanetary disks, including: Herbig, T Tauris, and transitional disks. Building on previous work, we classified CO emission into two fundamental line shapes, triangular and double-peaked. CO emission for each disk was then decomposed into a single or broad and narrow component. To systematically analyze this sample, these components were individually fit using a simple slab model that assumed LTE conditions for the gas, resulting in one T, N, and emitting area. These model fits replace previously analyzed line ratios that were used as proxies for rotational excitation, vibrational excitation, and column density (Banzatti et al. 2022). Throughout analysis we have identified several trends in the slab model results with known disk and stellar parameters:

- T(v1) and M_{Star} : anti-correlation; potential interpretation: CO at larger radii in more massive stars (supported by R_{CO} plot in Figure 32), the gas will also be colder.
- T(v1) and R_{CO} : anti-correlation; interpretation: closer-in gas is hotter gas.
- N(v1) and M_{Star}/L_{Acc} : decreasing up to $\sim 1 M_{\odot}$, then increasing; potential interpretation: currently unknown.
- N(v1) and n_{13-30} : anti-correlation; interpretation: gas is depleted when inner disk dust is depleted.
- T(v1) and n_{13-30} : anti-correlation; interpretation: dust depletion moves CO to larger radii, and therefore colder T.

Future work

Moving forward with the expansion of this IRTF-iSHELL survey will aid in providing a more complete overview of diverse excitation conditions and trends.

Increasing the detections of $^{12}\text{CO } \nu = 2 - 1$ and $^{13}\text{CO } \nu = 1 - 0$ in combination with

measured system properties will help to better describe the regions and conditions where different line types and velocity components may trace in disks. Further detailed study of CO emission with iSHELL will support analysis of future JWST CO spectra.

REFERENCES

- Abernathy, K., Banzatti, A., Jensen, S., Brittain, S., Boogert, A., Rayner, J., & Bruderer, S. (2021). An IRTF-iSHELL Survey of 4.52-5.25 μm CO Spectra in Protoplanetary Disks of Intermediate-mass Stars: Preliminary Sample and Analysis. *Research Notes of the American Astronomical Society*, 5(4), 80.
- Andrews, S. (2020). Observations of Protoplanetary Disk Structures. *arXiv*, 58, 483-528.
- Armitage, P. (2010). *Astrophysics of Planet Formation*. Cambridge Univ. Press.
- Brittain, S., Simon, T., Najita, J., & Rettig, T. (2007). Warm Gas in the Inner Disks around Young Intermediate-Mass Stars. *ApJ*, 659(1), 685-704.
- Bosman, A., Banzatti, A., Bruderer, S., Tielens, A., Blake, G., & van Dishoeck, E. (2019). Probing planet formation and disk substructures in the inner disk of Herbig Ae stars with CO rovibrational emission. *ApJ*, 631, A133..
- Brown, J., Pontoppidan, K., van Dishoeck, E., Herczeg, G., Blake, G., & Smette, A. (2013). VLT-CRIRES Survey of Rovibrational CO Emission from Protoplanetary Disks. *ApJ*, 770(2), 94..
- Carmona, A. (2010). Observational Diagnostics of Gas in Protoplanetary Disks. *Earth Moon and Planets*, 106(2-4), 71-95.
- Cushing, M., Vacca, W., & Rayner, J. (2004). Spextool: A Spectral Extraction Package for SpeX, a 0.8-5.5 Micron Cross-Dispersed Spectrograph. *PASP*, 116(818), 362-376.
- Dauphas, N., & Chaussidon, M. (2011). A Perspective from Extinct Radionuclides on a Young Stellar Object: The Sun and Its Accretion Disk. *Annual Review of Earth and Planetary Sciences*, 39, 351-386.
- Espaillet, C., Muzerolle, J., Najita, J., Andrews, S., Zhu, Z., Calvet, N., Kraus, S., Hashimoto, J., Kraus, A., & D'Alessio, P. (2014). An Observational Perspective of Transitional Disks. In *Protostars and Planets VI* (pp. 497-520).
- Herczeg, G., Brown, J., van Dishoeck, E., & Pontoppidan, K. (2011). Disks and outflows in CO rovibrational emission from embedded, low-mass young stellar objects. *ApJ*, 533, A112.

- Goldsmith, P., & Langer, W. (1999). Population Diagram Analysis of Molecular Line Emission. *apj*, 517(1), 209-225.
- Larsson, B., Liseau, R., & Men'shchikov, A. (2002). The ISO-LWS map of the Serpens cloud core. II. The line spectra. *ap*, 386, 1055-1073.
- LibreTexts (2023, January 30). *Rovibrational Spectroscopy*. LibreTexts Chemistry. [https://chem.libretexts.org/Bookshelves/Physical_and_Theoretical_Chemistry_Textbook_Maps/Supplemental_Modules_\(Physical_and_Theoretical_Chemistry\)/Spectroscopy/Rotational_Spectroscopy/Rovibrational_Spectroscopy](https://chem.libretexts.org/Bookshelves/Physical_and_Theoretical_Chemistry_Textbook_Maps/Supplemental_Modules_(Physical_and_Theoretical_Chemistry)/Spectroscopy/Rotational_Spectroscopy/Rovibrational_Spectroscopy)
- Miotello, A., Kamp, I., Birnstiel, T., Cleeves, L., & Kataoka, A. (2022). Setting the Stage for Planet Formation: Measurements and Implications of the Fundamental Disk Properties. *arXiv e-prints*, arXiv:2203.09818.
- Najita, J., Carr, J., & Mathieu, R. (2003). Gas in the Terrestrial Planet Region of Disks: CO Fundamental Emission from T Tauri Stars. *apj*, 589(2), 931-952.
- Salyk, C., Blake, G., Boogert, A., & Brown, J. (2009). High-resolution 5 μ m Spectroscopy of Transitional Disks. *apj*, 699(1), 330-347.
- Salyk, C., Blake, G., Boogert, A., & Brown, J. (2011). CO Rovibrational Emission as a Probe of Inner Disk Structure. *apj*, 743(2), 112.
- Sánchez, M. A. (2021). *A Study of Protoplanetary Disk Evolution in Infrared CO Emission* [Master's Thesis, Texas State University].
- Stahler, S., & Palla, F. (2004). *The Formation of Stars*. Wiley-VCH.
- van der Plas, G., Ancker, M., Waters, L., & Dominik, C. (2015). The structure of disks around Herbig Ae/Be stars as traced by CO ro-vibrational emission. *ap*, 574, A75.